ABSTRACT

Title of dissertation: SCATTERING FROM CHAOTIC CAVITIES: EXPLORING THE RANDOM COUPLING MODEL IN THE TIME AND FREQUENCY DOMAINS

James Hart, Doctor of Philosophy, 2009

Dissertation directed by: Professor Edward Ott
Professor Thomas Antonsen
Department of Physics

Scattering waves off resonant structures, with the waves coupling into and out of the structure at a finite number of locations ('ports'), is an extremely common problem both in theory and in real-world applications. In practice, solving for the scattering properties of a particular complex structure is extremely difficult and, in real-world applications, often impractical. In particular, if the wavelength of the incident wave is short compared to the structure size, and the dynamics of the ray trajectories within the scattering region are chaotic, the scattering properties of the cavity will be extremely sensitive to small perturbations. Thus, mathematical models have been developed which attempt to determine the statistical, rather than specific, properties of such systems. One such model is the Random Coupling Model.

The Random Coupling Model was developed primarily in the frequency domain. In the first part of this dissertation, we explore the implications of the Random Coupling Model in the time domain, with emphasis on the time-domain behavior of the power radiated from a single-port lossless cavity after the cavity has been

excited by a short initial external pulse. In particular, we find that for times much larger than the cavity's Heisenberg time (the inverse of the average spacing between cavity resonant frequencies), the power from a single cavity decays as a power law in time, following the decay rate of the ensemble average, but eventually transitions into an exponential decay as a single mode in the cavity dominates the decay. We find that this transition from power-law to exponential decay depends only on the shape of the incident pulse and a normalized time.

In the second part of this dissertation, we extend the Random Coupling Model to include a broader range of situations. Previously, the Random Coupling Model applied only to ensembles of scattering data obtained over a sufficiently large spread in frequency or sufficiently different ensemble of configurations. We find that by using the Poisson Kernel, it is possible to obtain meaningful results applicable to situations which vary much less radically in configuration and frequency. We find that it is possible to obtain universal statistics by redefining the radiation impedance parameter of the previously developed Random Coupling Model to include the average effects of certain classical trajectories within the resonant structure. We test these results numerically and find good agreement between theory and simulation.

SCATTERING FROM CHAOTIC CAVITIES: EXPLORING THE RANDOM COUPLING MODEL IN THE TIME AND FREQUENCY DOMAINS

by

James Aamodt Hart

Dissertation submitted to the Faculty of the Graduate School of the
University of Maryland, College Park in partial fulfillment
of the requirements for the degree of
Doctor of Philosophy
2009

Advisory Committee:
Professor Edward Ott, Chair/Advisor
Professor Thomas Antonsen, Co-Advisor
Professor Steven Anlage
Professor Thomas Murphy
Professor Brian Hunt

Dedication

To my parents, who worked so hard to raise me right:

Grant and Deborah Hart

Acknowledgments

I would like to acknowledge the vital assistance of Prof. Antonsen and Prof. Ott. They provided me with much needed support, feedback, and guidance during my time as a PhD student. Without their help, I would never have seen the opportunities available or found the techniques needed to solve the problems in my research. In addition, I would like to thank Prof. Anlage for both his unwavering support and for access to his laboratory. I would also like to thank John Rodgers for the brief loan of his computer. It saved an enormous amount of time.

I would also like to thank my coworkers willing to test my theoretical predictions, including Jen-Hao Yeh, Elliot Bradshaw and Sammer Hemmady. Without their feedback and constant work, my results would be far less trustworthy.

I would also like to give special thanks to Richard Prange, whose theoretical insights and techniques proved vital to the theory developed in this dissertation. May he rest in peace.

I would also like to thank Brian Hunt and Thomas Murphy for being on my doctoral defense committee. In addition, I would like to thank my friends Nicholas Mecholsky, Matthew Cornick, Kate Despain, Biniyam Taddesse, Cijan Kurter, Laura Adams and Florian Schaefer for their support and encouragement over the years.

I would also like to thank my parents for their dedicated support throughout my life. I would never have made it here without them. Thank you all!

Table of Contents

List of Figures

Chapter 1

Introduction

Waves are a ubiquitous part of the physical world. In fact, at the most fundamental level, all particles are described by quantum mechanics and are thus essentially waves. Even at the macroscopic level, many useful and important phenomena are waves, including such varied phenomena as electromagnetic waves, acoustic waves, waves on the surface of water, etc. Thus, describing wave phenomena is important and useful in many different fields of physics, both theoretical and applied.

While there are many different types of waves, a large number of wave problems can be modeled by a variant of the linear, scalar wave equation (also known as the Helmholtz equation),

$$\left(\nabla^2 + k^2\right)\psi(\vec{r}) = 0, \tag{1.1}$$

where ψ represents the wave field and $k = 2\pi/\lambda$, where λ is the wavelength of the wave. For instance, Eq. (1.1) is equivalent to Schrödinger's equation in empty space

$$i\hbar\frac{\partial}{\partial t}\Psi(\vec{r},t) = -\frac{\hbar^2}{2m}\nabla^2\Psi(\vec{r},t) \tag{1.2}$$

via the ersatz

$$\Psi(\vec{r},t) = \psi(\vec{r})e^{-i\hbar k^2 t/2m}. \tag{1.3}$$

In the appropriate regimes, Eq. (1.1) can also be applied to acoustic waves in matter, waves on the surface of various media, and electromagnetic waves systems which allow only quasi-2D dynamics. Via simple modifications, Eq. (1.1) can be applied

to an even larger range of problems. For instance, if the density of a medium (or the applied potential) is not uniform, k can be modified to be a function of $\vec{r}$. In the case of electromagnetism, a form of Eq. (1.1) can be found, but with ψ as a vector rather than a scalar. In the case of uniform loss or gain, the simple ersatz $k \to k + i\alpha$, where $\alpha = k/(2Q)$ and $Q \gg 1$ is the loss parameter of the closed cavity, successfully predicts a system's behavior. If there are sources or sinks within the system, it is necessary to add inhomogeneous terms to the right side of Eq. (1.1).

Therefore, solving Eq. (1.1) is an extremely practical and common problem. However, Eq. (1.1) cannot be solved without specifying boundary conditions. The shape of the boundary can be, and in practical applications quite often is, quite irregular. This is a very difficult problem in general; the well-known solutions to Eq. (1.1) are found in simple geometries which are rarely encountered in any cases except those specifically engineered to have the required symmetry. Often, such careful engineering is not possible, either because of other constraints or because we have no control over the properties of the system of interest. Thus methods of solving Eq. (1.1) in general, both numerically and theoretically, are of broad interest and are still being actively researched.

Solving Eq. (1.1) in general has other theoretical implications. For instance, from the correspondence principle, the dynamics of quantum mechanical systems must become equivalent to those of classical mechanics as the wavelength of the particles in the system become very small. However, the classical limit can have some extraordinary properties. For instance, the classical limit can often have chaotic dynamics, in which initially close classical trajectories diverge exponentially in time.

It is impossible for the solutions of Eq. (1.1) to diverge exponentially in time; each eigenmode simply oscillates independently with a fixed frequency in time, resulting in very simple, linear dynamics. This is not a paradox because the relationship between classical trajectories and quantum eigenstates is not trivial. In fact, relationships between several quantum-mechanical properties and classical trajectories have been found, especially in the short-wavelength limit. In general, the properties of quantum mechanical systems whose classical limit is chaotic are distinct from those same systems who classical limit is integrable.

One common class of well-studied systems whose classical limit is chaotic are chaotic billiards. Billiards are classical systems with some well-defined boundary. Classical particles within the boundary travel at constant velocities. When they are incident on the boundary, the classical particles reflect specularly. In many such systems, the dynamics of these classical particles have been proven to be chaotic. Some common chaotic billiards are shown in Fig. 1.1. The quantum-mechanical analogue of classical billiards are the higher-dimensional versions of the infinite square well, with the potential zero inside the boundary, and infinite on and outside the boundary. From a theoretical standpoint, these systems are very useful for testing the various theories and methods that have been proposed to solve Eq. (1.1). In practice, however, it is challenging to create quantum-mechanical systems with the desired attributes. Thus alternative macroscopic systems that obey Eq. (1.1) with constant k are desirable. Such macroscopic analogues exist, and include acoustic and electromagnetic cavities.

The electromagnetic analogues of such systems are cavities filled with a uni-

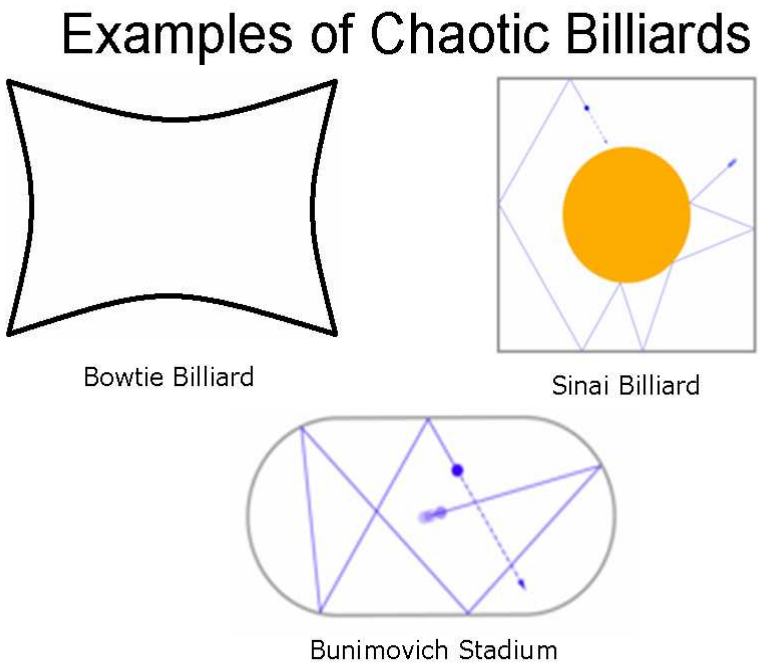

Figure 1.1: Several examples of billiards whose ray trajectories have chaotic dynamics.

form, isotropic, lossless, linear dielectric and bounded by a perfect conductor. The electromagnetic case is more difficult than the quantum mechanical because of the vector nature of the electric and magnetic fields. However, if we constrain the cavity to be much narrower than the wavelength in the z-direction, then the resulting propagating modes are uniform in the z-dimension, and obey the 2D Helmholtz equation in the x-y plane, with the electric field (which is purely in the z direction) constrained to be zero on the two-dimensional boundary [52]. Thus using macroscopic, electromagnetic cavities, it is possible to test theoretical predictions for quantum-mechanical systems.

Many theoretical connections have been made between classical orbits and the corresponding quantum-mechanical properties [31, 32, 8]. These connections have proven extremely fruitful, but have limits. For instance, in chaotic systems, it is challenging to numerically find and classify all periodic orbits (a common element of the semi-classical approach to wave chaos) due to their rapid proliferation and high sensitivity to initial conditions. In addition, any experimental setup created to model such a system will invariably deviate from the ideal theoretical setup, and the resulting changes, combined with the chaotic sensitivity, will make any results disagree quantitatively, even while agreeing qualitatively. Thus, in practice, most theories do not attempt to predict exact results, but rather aim to predict the statistical properties of such observable quantities as the spectrum [56], the eigenfunctions, the scattering amplitudes [19, 43, 18, 42], and other related measurements. The statistical approach is the approach we take here.

There are two broad methods used to predict the statistical behavior of wave

chaotic systems. One is the semiclassical method, treating the length and stability of the classical trajectories as statistical quantities or theoretical inputs [30, 4, 6]. The other is random matrix theory, a set of mathematical tools designed to predict the generic properties of complex wave or quantum systems without including any details [32, 56, 19, 43, 18]. These methods are generally complementary, and we will combine elements of both to make our predictions. The core of our results, however, lie within random matrix theory. Specifically, they lie within a branch of random matrix theory that has been developed more recently, known as the random coupling model. Thus we first turn our attention to random matrix theory, and then the random coupling model as developed in the context of random matrix theory.

1.1 Random matrix theory

Random matrix theory is based on the premise that sufficiently complex wave systems have a wide range of properties that are generic, i.e., not dependent on the details of the system being modeled, but rather dependent only on the underlying physical symmetries. This premise has been tested in many different contexts and has proved remarkably accurate in many of them, although this fact is considered remarkable even by those who have extensive experience with the field [31].

Random matrix theory was originally developed and applied in the field of nuclear physics by Wigner [56], who used it to model the spectra of nuclei excited by incident neutrons. This development was spurred by the (at that time) lack of a dynamical theory for the strong interactions, as well as various theoretical

considerations suggesting that such a model might be appropriate. In this context many important concepts, such as the basic symmetry classifications, the Gaussian and Circular ensembles, the level-spacing statistics, and the eigenvector statistics were derived [32].

Later, it was found that many other systems could also be characterized with random matrix theory, such as chaotic quantum systems [8], disorganized media, or quantum networks [27, 39, 38]. In addition, new mathematical techniques such as supersymmetry [32] were discovered which enabled much more complex quantities to be evaluated in the context of random matrix theory. With these developments, the field of random matrix theory has grown enormously, and remains an invaluable tool for analysis of complex systems.

Random matrix theory is used in practice by taking a wave system with unknown or complex dynamics and treating the pertinent operator (typically the Hamiltonian or a scattering matrix) as an element of an ensemble of N-dimensional random matrices, where N is large but finite. The classical random matrix ensembles defined by Wigner [56] and Dyson [19] are constrained only by the known physical symmetries and are otherwise assumed to be completely random. Later work has produced ensembles which have some additional constraints (such as non-zero averages or a banded structure) but are otherwise assumed to be random [29]. Which ensemble is appropriate must be determined by considerations outside of random matrix theory.

One type of statistic that demonstrates how random matrix theory is used is the nearest level spacing statistic [32]. Any sufficiently complex, confined wave

system will have a countably infinite set of eigenenergies. One question of interest with respect to these eigenenergies is how they are distributed with respect to each other, i.e., how closely spaced are they. The average spacing between eigenvalues is something that cannot be modeled by random matrix theory; it is not generic. This can be easily seen by noting that such an average level spacing depends on the units in which energy is measured. It must be determined experimentally or predicted using outside knowledge of the system. On the other hand, the energy level differences between adjacent eigenvalues within a narrow energy band, once normalized to the average spacing, can be predicted by random matrix theory. Although the experimental systems have an infinite, deterministic spectrum, and the ensembles are finite-dimensional and random, the local eigenvalue spacing statistics are typically found to be very accurately the same for both. Other predictions by random matrix theory are of a similar nature; once the system-specific properties have been specified, the behavior of purely random ensembles mirrors that of complex systems.

The energy-level statistics are of especial interest to those interested in wave chaos because the statistical properties of the level spacings are radically different for wave systems whose ray equations are integrable rather than chaotic. Of particular interest is the fact that random matrix theory predicts that energy levels will repel each other. In other words, the probability density of the spacing of two adjacent eigenenergies goes to zero as the spacing goes to zero (i.e., the probability of near degeneracy is very low). In integrable systems, on the other hand, no such effect occurs; eigenenergies being almost degenerate is extremely common and not suppressed [31, 32].

1.2 Types of Random Matrices

1.2.1 Symmetries and Ensembles

There are constraints on the Random Matrices that can be used to model various physical systems. For instance, if the system being modeled has an axis of symmetry (as with all of the billiards in Fig. 1.1), the eigenfunctions of the resulting system will be cleanly divided into independent symmetric and anti-symmetric solutions. The resulting Hamiltonian is block-diagonal, with the symmetric solutions in one block and the anti-symmetric solutions in the other. In general, all symmetries will produce this blocked behavior, with a separate block for each quantum number of the symmetry. Random matrix theory handles these symmetries by treating each block as a random matrix independent of all other blocks. Two eigenvalues from separate blocks do not experience level repulsion, although the eigenvalues within each block do. Such symmetries mix the resulting spectra and destroy the measurable level spacing repulsion. Most tests of random matrix theory reduce the symmetry so that only one block Hamiltonian is measured.

In addition, the behavior of the system under time-reversal constrains the possible Hamiltonians or other operators. This is not a geometric symmetry like the ones described in the previous paragraph, in that there is no quantum number associated with the symmetry, and the matrices cannot be decomposed into block-diagonal form. Instead, the structure of the various matrices is constrained. Dyson showed [19] that there are three fundamental types of time-reversal behavior in quantum-mechanical systems, each one imposing structural constraints on

the resulting operators. The third symmetry group enumerated by Dyson (which produces the so-called symplectic ensembles) can exist only in systems which have half-integer spin and a few other technical constraints [19], and are very difficult to access experimentally, especially in macroscopic systems. Thus, in this dissertation, we ignore the symplectic case and consider only the other two readily accessible time-reversal categories, which are

1. systems with time-reversal invariance, which result in the various Orthogonal ensembles,

2. and systems whose time-reversal invariance has been broken, which result in the various Unitary ensembles.

In addition to these three classes, there are intermediate states in which (for example) time-reversal invariance has been broken, but only very weakly, or only in a small part of the system. These intermediate states are still not well understood, and are the subject of active research [45, 32, 1, 44, 50].

Each of these classes results in different constraints on the elements of the ensembles. The Helmholtz equation (Eq. (1.1)) falls in class 1 and is where we will focus the bulk of our numerical and experimental effort.

These different classes of ensembles are often closely related to each other. In fact, the equations describing them are often analytically identical if we introduce β, an integer which indexes the type of ensemble being considered. For the Orthogonal(Unitary, Symplectic) Ensembles, we have $\beta = 1(2, 4)$.

1.2.2 The Gaussian Ensembles

The Gaussian Ensembles were the first random matrix ensembles to be applied to solve physical problems [56, 2, 29, 32]. The elements of the Gaussian Ensembles, which we denote $\boldsymbol{H}$, are used to model the Hamiltonians of closed systems and thus are Hermitian. For the symmetry classes defined in Sec. 1.2.1,

1. systems with time-reversal invariance and rotational symmetry must have a real and symmetric $\boldsymbol{H}$, resulting in the Gaussian Orthogonal Ensemble (GOE),

2. systems whose time-reversal invariance has been broken must have an $\boldsymbol{H}$ which is Hermitian, resulting in the Gaussian Unitary Ensemble (GUE).

One of the primary requirements used to derive the Gaussian Ensembles is that they be basis independent [32]. In practice, this means that the distribution must be invariant under arbitrary changes of basis $\boldsymbol{H} \rightarrow \boldsymbol{U}\boldsymbol{H}\boldsymbol{V}$. In the Orthogonal case, $\boldsymbol{V} = \boldsymbol{U}^T$ and $\boldsymbol{U}$ is any orthogonal matrix. In the unitary case, $\boldsymbol{U}$ and $\boldsymbol{V}$ are independent, arbitrary unitary matrices. The second major constraint typically imposed is that they be as random as possible, e.g. that they be distributed in such a way as to maximize the information entropy associated with their distribution. With these constraints, the pdf of the Gaussian ensembles with respect to the Lebesgue measure on the matrix entries is found to be

$$P(\boldsymbol{H}) \propto exp\left(-\frac{\beta}{4}\mathrm{tr}(\boldsymbol{H}^2)\right), \tag{1.4}$$

which implies that every independent element of $\boldsymbol{H}$ is an *independent* Gaussian random variable centered on zero. In the GOE, the width of the diagonal elements

of $\boldsymbol{H}$ is twice that of the off-diagonal elements. In contrast, in the GUE case, the real and imaginary parts of the off-diagonal elements, as well as the diagonal elements, are all independent Gaussian random variables and all have the same width.

In many cases, the physical quantity of interest is not the individual elements of $\boldsymbol{H}$, but rather the eigenvalues, which we denote E_n. The distribution of the E_n is given by [32]

$$P(\{E_n\}) \propto exp\left(-\frac{\beta}{4}\sum_n E_n^2\right)\prod_{n<m}|E_n - E_m|^\beta. \tag{1.5}$$

Note that this pdf is a product of two factors, with the first one equivalent to the global properties expressed in Eq. (1.4) and the second dependent only on the pairwise difference between eigenvalues. This kind of distribution is typical of eigenvalues of random matrices of all sorts.

It is worth again mentioning that these ensembles are typically used to model fluctuations from non-generic behavior. The density of states for the Gaussian ensembles (e.g. the average number of eigenvalues between E and $E + dE$, where dE is an infinitesimal energy) are given by the Wigner semicircle distribution [32]

$$\rho(E) = \frac{1}{2\pi}\sqrt{4N - E_n^2}, \tag{1.6}$$

which depends explicitly on N, and thus cannot be used to model the density of states in any physical Hamiltonian, which typically has an infinite spectrum with the density of states determined by non-generic considerations. Rather, the spectrum so generated is typically unfolded (i.e. rescaled and shifted so that the density of states matches that of the target system) and then analyzed in terms of the statistics of the resulting physical properties.

Using the Gaussian ensembles, it is possible to model the scattering matrix of a chaotic system coupled to the outside world. In order to do this, however, it is necessary to specify the coupling between the scattering channels and the modes of the closed system. This coupling is typically not random but rather depends on the detailed properties of the method used to couple energy into and out of the system. Thus adding coupling typically requires adding information about the ports to the system.

1.2.3 The Circular Ensembles

The circular ensembles were first introduced to physics by Dyson [19]. They are used to model the scattering properties of ideally-coupled chaotic systems. They are unitary matrices. We denote the elements of this ensemble by $\boldsymbol{S}$. For the symmetry classes defined in Sec. 1.2.1,

1. systems with time-reversal invariance and rotational symmetry must have a symmetric $\boldsymbol{S}$, resulting in the Circular Orthogonal Ensemble (COE),

2. systems whose time-reversal invariance has been broken must have an $\boldsymbol{S}$ which is unitary, result in the Circular Unitary Ensemble (CUE).

In Sec. 1.2.2, we saw that the Gaussian Ensembles were constructed to be basis-independent. We impose the same constraint on the circular ensembles: Their pdf must be invariant under changes of basis, but the matrices must be otherwise random, once the appropriate time-invariant structure has been imposed.

For the CUE, these constraints have a deep meaning. The circular unitary ensemble forms a group under matrix multiplication ($U(N)$), and changes of basis correspond to left- or right-multiplying by other elements of the group. We are thus seeking a measure on the group of unitary matrices which is invariant under the transformation $\boldsymbol{S} \to \boldsymbol{USV}$, where $\boldsymbol{U}$ and $\boldsymbol{V}$ are arbitrary $N \times N$ unitary matrices. Because $U(N)$ is a compact group, such a measure exists and is unique; it is given by the Haar measure for $U(N)$ [55, 33], normalized so that the integral over the entire group is 1.

Clearly the explicit form of the Haar measure will vary depending on how one parameterizes the scattering matrices. For instance, for scattering matrices $\boldsymbol{S}$ distributed uniformly w.r.t the Haar measure, the resulting eigenvalues of $\boldsymbol{S}$, denoted $e^{i\phi_n}$, have the pdf [19, 32]

$$P(\{\phi_n\}) \propto \prod_{n<m} |e^{i\phi_n} - e^{i\phi_m}|^2. \tag{1.7}$$

The Haar measure is simply a geometric factor, and all elements of the group are equally likely when distributed according to the Haar measure. In a three-dimensional analogy, consider a sphere. Clearly every point on the surface of the sphere is identical to every other; if we rotate the sphere around its center in three dimensions, the surface does not change. If we wish to define a completely random distribution on the surface of the sphere, simply declaring every point identical is sufficient. However, in order to actually perform integrals over this distribution using spherical coordinates, it is necessary to introduce a geometric factor, which can be expressed $\sin(\theta)\, d\theta\, d\phi$, where θ is the inclination and ϕ is the azimuthal angle.

The Haar measure is the geometric factor defined on the group of unitary matrices and it depends on the choice of parametrization. The actual function whose entropy must be maximized to generate the Circular Ensemble is the *prefactor* to the Haar measure. The most random such prefactor is simply the function 1, and so the Haar measure describes the distribution of the elements of the CUE.

The elements of the COE do not form a group and therefore cannot be assigned a Haar measure. However, it is possible to parameterize the COE $\boldsymbol{S}$-matrices as [10]

$$\boldsymbol{S} = \boldsymbol{u}\boldsymbol{u}^T \tag{1.8}$$

where $\boldsymbol{u}$ is a unitary matrix chosen from the CUE. With this parametrization, we can see that all our constraints for the COE have been met. The resulting $\boldsymbol{S}$ will be symmetric, unitary and its pdf is invariant under changes of basis $S \to \boldsymbol{O}\boldsymbol{S}\boldsymbol{O}^T$, where $\boldsymbol{O}$ is an arbitrary $N \times N$ orthogonal matrix. That it is otherwise as random as possible can be seen by noting that beyond the symmetry constraints, we have added no information to the pdf. The resulting distribution of the eigenvalues of $\boldsymbol{S}$ for the COE is

$$P(\{\phi_n\}) \propto \prod_{n<m} |e^{i\phi_n} - e^{i\phi_m}|, \tag{1.9}$$

which is again simply a geometric factor. The function with maximized entropy is again 1.

1.2.4 The Poisson Kernel

In general, chaotic systems are not ideally coupled to the outside world and are not described by the circular ensembles. In effect, the assumptions behind our

use of the circular ensembles are incorrect; we do know something about the system and therefore the resulting scattering matrices are, in effect, less random. This can be seen by considering the discussion about the Gaussian ensembles; once we have assumed a random spectrum, we must still add information about the coupling into and out of the cavity in order to get a working model for a scattering system. In addition, the dynamics within the cavity once the signal has entered are often not random, but easily predicted from the presence of features near the coupling region. All of these effects lead to the breakdown of the Circular ensembles as useful descriptions of the scattering matrix.

To solve these problems, we need a new ensemble of scattering matrices [43]. The new distribution is based the maximum entropy principle with the constraint that the scattering matrix have a non-zero average $\bar{\boldsymbol{S}}$. The resulting distribution has the useful property that for any polynomial in the elements of $\boldsymbol{S}$ (but *not* allowing complex conjugation),

$$\langle S_{i,j} S_{k,l} \ldots \rangle = \bar{S}_{i,j} \bar{S}_{k,l} \ldots \tag{1.10}$$

where the brackets indicate ensemble averaging. The pdf w.r.t the Haar measure of the distribution of an $N \times N$ scattering matrix $\boldsymbol{S}$ with a symmetry indexed by β is then given by

$$P_{\bar{\boldsymbol{S}}}(\boldsymbol{S}) = \frac{1}{2^{N(\beta N+2-\beta)/2} V} \frac{\det\left(\mathbf{1} - \bar{\boldsymbol{S}}^\dagger \bar{\boldsymbol{S}}\right)^{(\beta N+2-\beta)/2}}{\det\left(\mathbf{1} - \bar{\boldsymbol{S}}^\dagger \boldsymbol{S}\right)^{\beta N+2-\beta}}. \tag{1.11}$$

The Poisson kernel represents a much broader set of systems than the circular ensemble. It not only allows for a prompt reflection from the port due to the mismatch between the port and the cavity, but also can model such features as direct

orbits between ports, the effects of nearby walls, whispering gallery trajectories, and so on [41, 42]. In effect, as long as the long-time behavior of the waves within the system become chaotic, the Poisson kernel can handle the short-term non-chaotic behavior.

Unlike the previous ensembles, the Poisson kernel is not invariant under changes of basis. Rather, it has the property [9]

$$P_{\bar{\boldsymbol{S}}}(\boldsymbol{USV}) = P_{\boldsymbol{U}\bar{\boldsymbol{S}}\boldsymbol{V}}(\boldsymbol{S}), \tag{1.12}$$

where in the presence of time-reversal invariance (corresponding to the orthogonal ensembles), $\boldsymbol{V} = \boldsymbol{U}^T$ with $\boldsymbol{U}$ being an arbitrary orthogonal matrix, and in the absence of time-reversal invariance, $\boldsymbol{U}$ and $\boldsymbol{V}$ are arbitrary unitary matrices.

Although the Poisson kernel can be used to model systems with poor coupling between the scattering channels and the system, it is not the most elegant method for modeling this behavior, relying as it does on the distribution of scattering matrices rather than the individual scattering matrices actually measured. The impedance matrices do a much better job of explicitly separating the non-random and random components of the scattering properties.

1.2.5 The Lorentzian Ensembles

The Lorentzian ensembles were originally used by Brouwer to represent Hamiltonians, but they can be used just as effectively to represent the impedance matrix of a scattering system. In fact, although he did not interpret it as such at the time, Brouwer's 1995 paper proved the mathematical equivalence of the Poisson kernel

description of the scattering matrix and the random coupling model description of the impedance [9].

The pdf of the Lorentzian ensemble with the symmetry determined by β is given by

$$P(\boldsymbol{H}) = \frac{1}{V} \frac{\lambda^{N(\beta N+2-\beta)/2}}{\det(\lambda^2 \mathbf{1} + (\boldsymbol{H} - \epsilon \mathbf{1})^2)^{(\beta N+2-\beta)/2}} \tag{1.13}$$

where V is a normalization constant which is independent of λ and ϵ, where λ and ϵ are the width and median, respectively, of the diagonal elements of $\boldsymbol{H}$, which are Lorenzian-distributed random variables. From Eq. (1.13), we can make the change of variables

$$\boldsymbol{H} = \lambda \boldsymbol{H}_0 + \epsilon \tag{1.14}$$

where $\boldsymbol{H}_0$ is a Lorentzian-distributed random matrix with width 1 and median 0 (e.g., $\boldsymbol{H}_0$ is distributed according to Eq. (1.13) with the parameters $\lambda = 1$ and $\epsilon = 0$). From Brouwer's work, we also have the result that

$$\boldsymbol{H}_0 = -i \frac{1 + \boldsymbol{S}}{1 - \boldsymbol{S}} \tag{1.15}$$

where $\boldsymbol{S}$ is distributed according to the circular ensemble with the same symmetry. As a result, for the Lorentzian Orthogonal Ensemble, the matrices are constrained to be symmetric. They also inherit the property that their distribution is basis independent in direct analogy to the basis-independence of the Gaussian and Circular ensembles.

The Lorentzian ensembles have the useful property that any diagonal submatrix of Lorentzian-distributed random matrices is also a Lorentzian distributed random matrix with identical λ and ϵ [9]. One corollary of this is that the diagonal

elements of a Lorentzian matrix are Lorentzian random variables. They also have the property that the inverse matrix $\boldsymbol{H}^{-1}$ is also a Lorentzian distributed random variable with $\lambda \to \lambda(\lambda^2 + \epsilon^2)^{-1}$ and $\epsilon \to \epsilon(\lambda^2 + \epsilon^2)^{-1}$.

From Eqs. (1.14) and (1.15) combined with the form of the eigenvalues of the circular ensembles, we get that the eigenvalues of the Lorentzian ensembles have the form $\lambda \cot(\phi_n/2) + \epsilon$, where the ϕ_n are distributed according to Eq. (1.7) or (1.9).

1.3 The random coupling model

Although many wave systems can be described by the Helmholtz equation, to probe such systems we must perform scattering experiments. This implies the need to model the coupling between the outside world and the scattering system. In general, the coupling between the wave system and the outside world is not universal, with a large part of the incident wave being reflected off the interface between the two without entering the chaotic system at all. We consider systems in which scattering can only occur through a small number of discrete channels coupled to the wave systems through discrete ports. In such cases, we find that we can separate the effects of coupling into and out of the system from those effects which occur within the system itself. Not all methods of describing the scattering factorize cleanly, however. One common method of characterizing the scattering behavior of a system is the $M \times M$ scattering matrix $\boldsymbol{S}$ where M is the number of scattering channels, but as discussed previously in our discussion of the Poisson kernel, the resulting model is not cleanly factorized into internal and external behavior. To get

this factorization, the appropriate formulation is the impedance matrix.

Impedance is a meaningful concept for all scattering wave systems. In linear electromagnetic systems, it is defined via the phasor generalization of Ohms law as

$$\hat{V} = \boldsymbol{Z}\hat{I} \tag{1.16}$$

where the M-dimensional vector $\hat{\boldsymbol{V}}$ represents the voltage differences across the attached transmission lines and the M-dimensional vector $\hat{\boldsymbol{I}}$ denotes the currents flowing through the transmission lines. The concept of impedance can be generalized to cases where the cavity is excited through an aperture in which case the impedance gives the components of the electric field in the place of the aperture in terms of the components of the magnetic field. In acoustics, the impedance is the ratio of the sound pressure to the fluid particles' velocity. The quantum-mechanical quantity corresponding to impedance is often denoted in the literature as $i\boldsymbol{K}$ [2].

Impedance can be related to the scattering matrix via the relationship [58, 59, 60]

$$\boldsymbol{Z} = \boldsymbol{Z}_0^{1/2}(\mathbf{1} + \boldsymbol{S})(\mathbf{1} - \boldsymbol{S})^{-1}\boldsymbol{Z}_0^{1/2}. \tag{1.17}$$

where $\boldsymbol{Z}_0$ is an $M \times M$ diagonal matrix whose ith diagonal element is the characteristic impedances of the ith scattering channel. In electromagnetic systems with transmission lines for scattering channels, the characteristic impedances are the ratio between the voltage difference across the transmission line and the current through the transmission line for a monochromatic wave propagating a single direction through the transmission line. Other wave systems have analogous definitions for $\boldsymbol{Z}_0$ determined by the details of the scattering channels.

In terms of impedance, the coupling strength between the scattering channels and the chaotic system is best expressed in terms of the $M \times M$ diagonal radiation impedance matrix $\boldsymbol{Z}_R$. The diagonal elements of $\boldsymbol{Z}_R$ are the radiation impedance of individual ports. The radiation impedance of a single port is the impedance that single transmission line would have if the system was configured such that any signal successfully transmitted through the port into the bulk of the cavity was immediately absorbed. The real and imaginary parts of $\boldsymbol{Z}_R$ are known as the radiation resistance and radiation reactance and are denoted $\boldsymbol{R}_R$ and $\boldsymbol{X}_R$, respectively.

In our work, we couple the outside world to the cavity by creating holes in the top of the quasi-2D cavity and inserting antennas attached to coaxial cables through them. We model the pth antenna as a phasor current with frequency f induced directly in the top plate of the cavity with a total current $\hat{I}_p$ and a shape $u_p(\vec{r})$, where $\vec{r}$ is a two-dimensional vector in the x-y plane. The current density $u_p(\vec{r})$ has the property that $\int d^2\vec{r} u_p(\vec{r}) = 1$ and we assume that the size of the current density is much smaller than a wavelength. With these additions, the Helmholtz equation becomes

$$\left(\nabla^2 + k^2\right) \psi(\vec{r}) = ikh\eta_0 \sum_{p=1}^{M} u_p(\vec{r}) \hat{I}_p, \tag{1.18}$$

where $k = 2\pi f$ is the wavenumber of the incident wave, h is the height of the cavity in the narrow dimension, $\eta_0 = \sqrt{\mu_0/\epsilon_0}$ is the characteristic impedance of waves within the cavity.

As we showed in previous work, the (n, m)th element of the port impedance

in a system described by Eq. (1.18) is given by

$$Z_{n,m} = i \sum_l \frac{kh\eta_0 \langle u_n \phi_l \rangle \langle u_m \phi_l \rangle^*}{k^2 - k_l^2} \tag{1.19}$$

where ϕ_n is the nth eigenfunction and k_n the nth eigenvalue of the closed system (e.g. $(\nabla^2 + k_n^2)\phi_n = 0$) and where $\langle \ldots \rangle$ is the integral over $\vec{r}$. The random coupling model's primary contribution is the result that the overlap integral $\langle u_n \phi_l \rangle$ can be statistically represented as

$$\langle u_n \phi_l \rangle = \sqrt{R_{R,n}(k_l)} w_l \tag{1.20}$$

where $R_{R,n}(k_l)$ is the radiation impedance of the nth port at frequency k_l and w_l is a Gaussian random variable width mean 0 and width 1. With this result, we found in previous work that [59, 60]

$$\boldsymbol{Z} = i\boldsymbol{X}_R + i\sqrt{\boldsymbol{R}_R}\boldsymbol{\xi}_0\sqrt{\boldsymbol{R}_R}, \tag{1.21}$$

The matrix $\boldsymbol{\xi}_0$ is an element of the appropriate $M \times M$ Lorentzian ensemble introduced by Brouwer [9] with width 1 and median 0, which in the single-port case simplifies to a Lorentzian random variable with width 1 and median 0. We denote $\boldsymbol{\xi}_0$ the normalized impedance and have extensively studied its properties in chaotic systems [58, 59, 60, 36].

Equations (1.19) and (3.4) were the primary results of our prior research and form the starting point for all research presented in this dissertation.

1.4 Outline of Dissertation

The dissertation is organized as follows: In Chapter 2[1], we show that the ensemble averaged power scattered in and out of lossless chaotic cavities decays as a power law in time for large times. In the case of a pulse with a finite duration, the power scattered from a single realization of a cavity closely tracks the power law ensemble decay initially, but eventually transitions to an exponential decay. We explore the nature of this transition in the case of coupling to a single port. We find that for a given pulse shape, the properties of the transition are universal if time is properly normalized. We define the crossover time to be the time at which the deviations from the mean of the reflected power in individual realizations become comparable to the mean reflected power. We demonstrate numerically that, for randomly chosen cavity realizations and given pulse shapes, the probability distribution function of reflected power depends only on time, normalized to this crossover time.

In Chapter 3[2], we extend Eq. (3.4) to ensembles whose statistics are not completely random. In particular, we find that if we consider the statistics of impedances generated by making small perturbations to a single baseline wave-chaotic cavity over a narrow frequency window, Eq. (3.4) is incorrect. However, we find that by defining a generalized radiation impedance $\boldsymbol{Z}_{avg}$ which includes the effects of short orbits within the cavity, we can replace $\boldsymbol{Z}_R$ in Eq. (3.4) with $\boldsymbol{Z}_{avg}$, where we can

[1]Chapter 2 is a republication of work published in Physical Review E, as approved by the thesis committee [35].

[2]Chapter 3 has been submitted for publication in Physical Review E and is available as a preprint, as approved by the thesis committee [34].

explicitly calculate $\boldsymbol{Z}_{avg}$ if we know the details of the scattering system.

Chapter 2

Long time scattering off single-port chaotic systems

In this chapter, we focus our efforts on understanding the long-time behavior of the power reflected off a wave-chaotic cavity whose scattering properties are well-described by the random coupling model as discussed in chapter 1. The scattering properties of such wave systems have been well studied, both experimentally [54, 20, 14, 15, 40, 7] and theoretically [46, 2, 29, 17, 3, 61, 13], in a wide variety of contexts. Much of the the theory has focused on the frequency domain, and sophisticated techniques exist to analyze and characterize the scattering process. See Refs. [2, 29, 17, 3, 61, 13] and the references cited therein. Similarly, the time domain response of typical wave systems to a delta-function impulse has also been considered [17, 3, 61, 13], especially in relationship to fidelity decay(for an overview of fidelity decay, see the Ref. [28] and the references therein). In this chapter, we consider an intermediate situation: we excite the wave system through an external port with a pulse modulated sinusoidal signal, exciting a large but finite number of modes. The problem of scattering pulse-modulated sinusoidal waves arises in a host of diagnostic situations, such as radar, sonar, nuclear scattering, etc. In what follows, for specificity, we discuss our problem in the context of electromagnetic waves. For simplicity, we consider only lossless two-dimensional microwave cavities excited through a small antenna. We emphasize that the results we obtain can

be generalized to higher-dimensional systems and to quantum mechanical or other wave-chaotic systems(e.g., acoustic or elastic wave systems).

On a formal level, the time domain dynamics of such a system is straightforward. The system is open and linear. An incident pulse with a small but finite width in the time domain excites a large number of modes in the cavity, which then radiate their energy back out through the port. Because the system is linear, the reflected voltage can be expressed as a superposition of contributions from modes of the open system. The chaotic dynamics is expressed, not through the dynamics of the individual modes, but rather in the eigenvalue statistics [31] and the statistics of the coupling between the port and the cavity.

As showed in Sec. 2.1, the contribution from each mode decays exponentially in time. For short times compared with the Heisenberg time (the inverse of the mean spacing of mode frequencies), the resulting dynamics will be determined primarily by the semiclassical dynamics within the cavity [49]. However, for large times compared with the Heisenberg time, the ensemble average of the reflected power decreases as a power law in time [17]. This is due to the fact that there is a probability distribution of mode decay rates which extends to zero decay rate, and for long times the average is dominated by modes with very small decay rates. In the case of a single realization of the chaotic cavity, the incident pulse excites a large number of modes with very similar amplitudes, and consequently the reflected power initially behaves as though the sum of modes were an ensemble average, and the total power decays as a power law. We call this behavior self-averaging. In a single specific realization, however, there are only a finite number of modes excited. Eventually the slowest-decaying

mode in the realization will be much larger than the other modes, and the sum will be dominated by this slowest mode, which decays exponentially. Thus for extremely long times we expect that the reflected power for any single realization will fall exponentially, eventually becoming much smaller than the ensemble average.

To test this hypothesis, we have created a program that models the time-domain behavior of generic chaotic systems. It does this by first generating the spectrum and coupling constants of a cavity using the Random Coupling Model [59] (RCM) and then integrating the evolution equations for fields in the cavity, which are modeled in the RCM as a set of driven, damped coupled harmonic oscillators. Single realizations of the power reflected from these cavities, as well as the ensemble average of 50 different cavities, are shown in Fig. 2.1, where we show two very different realizations: one (Fig. 2.1(a)) in which the self-averaging persists throughout the length of the time shown and one (Fig. 2.1(b)) in which self-averaging occurs early, but becomes dominated by solitary slowly decaying modes before the conclusion of the numerical simulation.

Our goal in this chapter is to quantitatively describe the transition from self-averaging to exponential decay. In particular, we wish to predict the time-scale needed to see this transition. In Sec. 2.1, we describe the time-domain model we use for our analysis. In Sec. 2.2, we find the probability distribution function of the decay rates of the open-cavity modes (for the slowest decaying modes in the cavity) as a function of the cavity's port reflection coefficient. In Sec. 2.3 we find the average, standard deviation and (indirectly) the higher-order moments of the reflected power as a function of time, and use these moments to derive a normalized time which,

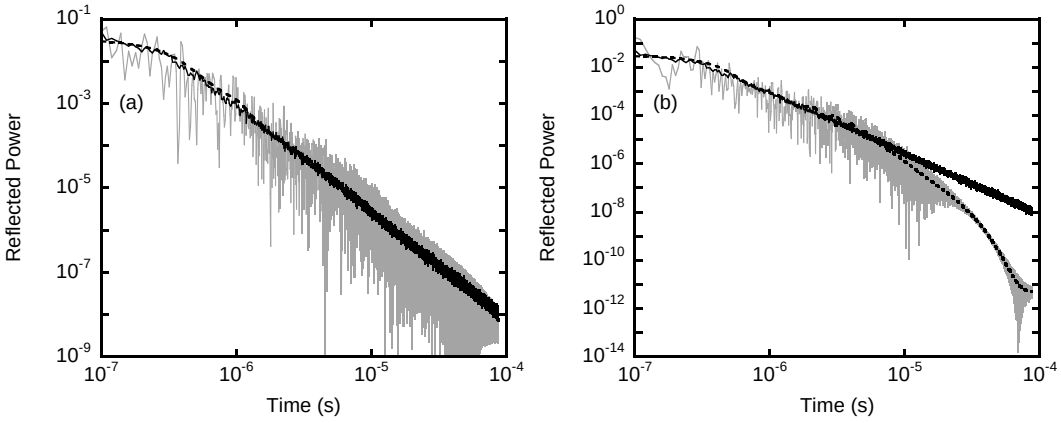

Figure 2.1: Using the Random Coupling Model (RCM), we created a program capable of simulating the time-domain response of an individual chaotic cavity to a pulse injected into the cavity through a small antenna. By repeatedly creating individual cavities using the RCM, we created an ensemble of such cavities. The gray lines represent the power reflected out of the cavity from two single realizations of the chaotic cavity. The dark solid line represents the reflected power averaged over 50 realizations of the chaotic cavity. The dashed line represents the time-averaged power for the single realization. Figure (a) represents a cavity where self-averaging persists throughout the entire simulation, but figure (b) is dominated by solitary modes after about 10^{-5} seconds.

along with the power spectrum of the incident pulse, is all that is needed to obtain a characterization of the transition from self-averaging to exponential decay. In Sec. 2.4, we evaluate the theory from Sec. 2.3 by numerically finding the number of modes which fall below certain fractions of the average, and we compare the theory with simulation results.

2.1 Model

We base our model system on that used in previous work [59]; specifically a quasi-two-dimensional, electromagnetic cavity defined by two conducting plates of area A separated by a distance h which are electrically connected along their perimeters by a conducting side-wall. The cavity is excited by an antenna that induces currents in the plates. The wave equation for this system is

$$\frac{1}{c^2}\frac{\partial^2}{\partial t^2}V_T - \nabla^2 V_T = h\mu u\frac{\partial I}{\partial t}, \tag{2.1}$$

where $c = (\epsilon\mu)^{-1/2}$ is the speed of propagation of waves in the uniform medium inside the cavity, ϵ and μ are the permittivity and permeability of this (non-dispersive) medium, $V_T(x, y)$ is the voltage difference between the plates, an antenna is modelled through the function $u(x, y)$ which gives the profile of current flowing in the antenna between the surfaces ($\int\int dx\, dy\, u(x, y) = 1$), and $I(t)$ is the time-dependent current driving the antenna. Further, as the side walls of the cavity are conducting, $V_T = 0$ along the perimeter of the cavity. A voltage $V(t)$ is induced at the terminals of the model antenna which is given in terms of the antenna profile u and V_T

$$V = \int dx\, dy\, uV_T. \tag{2.2}$$

The antenna is excited by an incident voltage pulse $V_{\rm inc}(t)$ arriving along a transmission line of characteristic impedance Z_0. The incident wave excites the cavity and produces a reflected wave pulse $V_{\rm ref}(t)$ travelling away from the cavity in the transmission line. At the junction between the transmission line and the cavity the voltages and currents at the antenna and on the transmission line match,

$$V(t) = V_{\rm inc}(t) + V_{\rm ref}(t), \tag{2.3}$$

$$I(t) = Z_0^{-1}[V_{\rm inc}(t) - V_{\rm ref}(t)]. \tag{2.4}$$

We now introduce Fourier transforms with transform frequency ω such that each time-dependent variable is represented in the following way,

$$V_T(x,y,t) = \int \frac{d\omega}{2\pi} e^{j\omega t} \bar{V}_T(x,y,\omega). \tag{2.5}$$

The transformed field within the cavity is then represented as a superposition of the orthonormal modes of the closed cavity,

$$\bar{V}_T(x,y,\omega) = \sum_n c_n(\omega)\phi_n(x,y). \tag{2.6}$$

where $(\nabla^2_{x,y} + k_n^2)\phi_n = 0$, and $\phi_n = 0$ on the cavity side walls.

Solving the transformed wave equation gives the amplitudes $c_n(\omega)$ which can then be inserted in Eq. (2.2) to find the transformed voltage,

$$\bar{V}(\omega) = \bar{I}(\omega) Z_e(\omega), \tag{2.7}$$

where

$$Z_e(\omega) = -j\sqrt{\frac{\mu}{\epsilon}} \sum_n \frac{kh}{k^2 - k_n^2} \left[\int dx\, dy\, u\phi_n \right]^2 \tag{2.8}$$

is the (exact) cavity impedance. Here k_n^2 are the eigenvalues of the closed cavity and $k = \omega/c$.

In Ref. [59, Eq. 14], it was shown that, if one assumed for the purpose of evaluating Eq. (2.8) that the eigenfunctions behave as if they were a superposition of random plane waves, the overlap between the eigenfunctions and antenna current profile could be expressed in terms of the radiation resistance of the antenna,

$$R_{rad}(k) = \frac{kh}{4}\sqrt{\frac{\mu}{\epsilon}}\int \frac{d\theta}{2\pi}|\bar{u}(\vec{k})|^2, \tag{2.9}$$

where $\bar{u}(\vec{k})$ is the spatial Fourier transform of the profile function $u(x, y)$, and the integral is over the angle θ of the vector $\vec{k}$.

Here $R_{Rad} = \mathrm{Re}[Z_{Rad}]$ where Z_{Rad}, the radiation impedance, is the impedance $\bar{V}(\omega)/\bar{I}(\omega)$ that would apply if the cavity side walls were moved to infinity and outward propagating radiation conditions were imposed.

With this random plane wave assumption, the exact impedance Z_e in Eq. (2.8) was replaced by a statistical model impedance,

$$Z(\omega) = -\frac{j}{\pi}\sum_n \frac{k\Delta w_n^2}{k^2 - k_n^2}\frac{R_{Rad}(k_n)}{k_n}, \tag{2.10}$$

where w_n are zero mean, unit variance, independent Gaussian random variables. It was further assumed in Ref. [59] that the eigenvalues k_n^2 have the statistical properties of eigenvalues of a Gaussian Orthogonal Ensemble (GOE) random matrix with mean spacing given by Weyl's formula,

$$\langle k_{n+1}^2 - k_n^2\rangle_n \equiv \Delta = 4\pi/A. \tag{2.11}$$

We now use the relationship (Eq. (2.7)) between the voltage $\bar{V}(\omega)$ and current

$\bar{I}(\omega)$ along with the transformed version of Eqs. ((2.3)) and ((2.4)) to find the transform of the reflected voltage pulse,

$$\bar{V}_{\text{ref}}(\omega) = \rho(\omega)\bar{V}_{\text{inc}}(\omega), \tag{2.12}$$

where the reflection coefficient $\rho(\omega)$ is given by

$$\rho(\omega) = \frac{Z(\omega) - Z_0}{Z(\omega) + Z_0}. \tag{2.13}$$

Although the derivation above has focused on the electromagnetic case, the expression Eq. (2.13) describes the reflection of a wide variety of waves when they hit an interface, viz., electromagnetic, acoustic, quantum mechanical, etc. The connection becomes closer when one considers, as we will, incident pulses whose transformed bandwidth ω_B is narrow enough that the radiation resistance and mean frequency spacing can be considered constant over the range of excited frequencies.

The time-dependence of the reflected pulse can be found by using the inverse Fourier transformation,

$$V_{\text{ref}}(t) = \int \frac{d\omega}{2\pi}\rho(\omega)\bar{V}_{\text{inc}}(\omega)e^{j\omega t}. \tag{2.14}$$

The long-term behavior of the reflected pulse is governed by the poles of $\rho(\omega)$ (denoted ω_k), which satisfy

$$Z_0 + Z(\omega_k) = 0. \tag{2.15}$$

The complex frequencies ω_k have positive imaginary parts as they correspond to decaying modes. We can approximate the long time dependence of the reflected pulse by pushing the inversion contour in Eq. (2.14) up into the upper half of the

ω-plane and deforming it around each pole

$$V_{\text{ref}}(t) = -2j \sum_k \frac{Z_0}{Z'(\omega_k)} \bar{V}_{\text{inc}}(\omega_k) e^{j\omega_k t}, \tag{2.16}$$

where $Z'(\omega_k) = dZ/d\omega|_{\omega=\omega_k}$. Thus, the long time behavior of $V_{\text{ref}}(t)$ is determined by the properties of eigenfrequencies ω_k of the open system. These eigenfrequencies have real values whose average spacing is denoted by $\Delta\omega$. In principle, $\Delta\omega$ can vary as a function of mode number. If we assume that the incident pulse has a spectrum centered at a carrier frequency ω_0, with a bandwidth $\omega_B \ll \omega_0$ we can relate $\Delta\omega$ to the mean spacing Δ of k_n^2 values

$$\Delta\omega = \frac{c^2\Delta}{2\omega_0}. \tag{2.17}$$

The inverse of this quantity can be identified with what is known as the Heisenberg time in the Quantum Chaos community.

Each mode has a decay rate $\gamma_k = \text{Im}(\omega_k)$ which varies from mode to mode. We denote the probability density function of these decay rates by $P_\gamma(\gamma)$. Considering the number of excited modes to be effectively finite, since each mode decays exponentially, the long time behavior of the reflected signal is dominated by modes with the smallest values of γ_k. From Eq. (2.15), along with the expression for $Z(\omega)$ in Eq. (2.10), it can be seen that these weakly coupled modes will have particularly small w_n and thus $\text{Re}(\omega_k) \simeq k_n c$. Given this observation, we can approximate the complex mode frequencies ω_n by solving for the poles in the weak coupling approximation. Specifically, in Eq. (2.10), our expression for the impedance, we separate

the term with $\omega_n \simeq k_n c$ from the others,

$$Z(\omega_n) = jX_n - j\frac{R_{Rad}(\omega_0)\Delta\omega w_n^2}{\pi(\omega_n - k_n c)}, \tag{2.18}$$

where we have changed our indexing labels from k to n (because every k_n has a corresponding ω_n), and

$$X_n = -\frac{1}{\pi}\sum_{n'\neq n}\frac{k_n w_{n'}^2 \Delta}{k_n^2 - k_{n'}^2}\frac{R_{Rad}(k_{n'})}{k_{n'}}. \tag{2.19}$$

Thus, we can solve Eq. (2.15) approximately for the complex mode frequencies,

$$\frac{\omega_n - k_n c}{\Delta\omega} = jw_n^2\frac{R_{Rad}}{\pi(Z_0 + jX_n)}. \tag{2.20}$$

From this we obtain an expression for the decay rate,

$$\gamma_n = \Delta\omega w_n^2\frac{R_{Rad}Z_0}{\pi(Z_0^2 + X_n^2)}. \tag{2.21}$$

The reactance X_n, like the impedance Z is a statistical quantity. It has an average value to which all the terms in Eq. (2.19) contribute, and which can be calculated by replacing the sum by an integral [59],

$$\langle X_n\rangle = X_{Rad} = -\frac{1}{\pi}P\left\{\int_0^\infty dk_{n'}^2\,\frac{k_n}{k_{n'}}\frac{R_{Rad}(k_{n'})}{k_n^2 - k_{n'}^2}\right\}. \tag{2.22}$$

where the symbol P indicates that principal value definition of the the integral is to be taken. This average value is the radiation reactance of the antenna. The reactance X_n has a fluctuating part which scales as the radiation resistance and is due primarily to terms in the sum where n and n' are not too different,

$$X_n = X_{Rad} + R_{Rad}\xi_n. \tag{2.23}$$

The quantity ξ_n has a universal distribution which we will investigate in depth later.

Using Eqs. ((2.18)) and ((2.20)) we may evaluate $Z'(\omega_n)$ in the denominator of Eq. (2.16). The result for the reflected signal is

$$V_{\rm ref}(t) = -2\sum_n \frac{Z_0 R_{Rad}}{(Z_0 + jX_n)^2} w_n^2 e^{j\omega_n t} \Delta\omega \bar{V}_{\rm inc}(\omega_n). \tag{2.24}$$

Taking the magnitude of this, we obtain the reflected power,

$$P_{\rm ref}(t) = \bar{P}_{\rm ref}(t) + \tilde{P}_{\rm ref}(t), \tag{2.25}$$

where

$$\bar{P}_{\rm ref}(t) = \sum_n \frac{\left|2\pi\Delta\omega \bar{V}_{\rm inc}(\omega_n)\right|^2}{Z_0} \frac{\gamma_n^2}{\Delta\omega^2} e^{-2\gamma_n t}, \tag{2.26a}$$

$$\tilde{P}_{\rm ref}(t) = \sum_{n,m\neq n} \frac{\left|2\pi\Delta\omega\right|^2 \bar{V}_{\rm inc}(\omega_n)\bar{V}^*_{\rm inc}(\omega_m)}{Z_0} \frac{\gamma_n\gamma_m}{\Delta\omega^2} e^{j(\omega_n - \omega_m^*)t} e^{2j(\psi_m - \psi_n)}, \tag{2.26b}$$

and ψ_n is the phase of $Z_0 + jX_n$.

The two contributions to the reflected power (2.26a) and (2.26b) are very different. In the first contribution the terms decay exponentially and smoothly and the sum is always positive. In fact, if we smooth over a timescale longer than the Heisenberg time, this first term will remain essentially unchanged. The second term, on the other hand, oscillates rapidly on a timescale comparable to the Heisenberg time, but tends to zero if averaged over long timescales. For the very long timescales needed to see the transition from self-averaging to exponential decay, we can treat the rapidly fluctuating terms in $P_{\rm ref}(t)$ as random variables with the phases in the exponents $((\omega_n - \omega_m^*)\,t)$ being uniformly distributed. Under this assumption, we find that, for a single realization of the chaotic cavity, the fluctuating part of $P_{\rm ref}$ is random and has a variance of

$$\sigma^2 = \langle \left[\tilde{P}_{\rm ref}(t)\right]^2 \rangle_t \leq \bar{P}^2_{\rm ref}(t). \tag{2.27}$$

where $\langle \ldots \rangle_t$ indicates a sliding averaging in t over a timescale that is long compared to the Heisenberg time but short compared to the characteristic time for variation of $\bar{P}_{\rm ref}(t)$. That is, the order of magnitude of the oscillating part of $P_{\rm ref}$ is typically the same as that of the smoothed part. Thus, if the smoothed part of $P_{\rm ref}$ drops exponentially, the fluctuations around it will as well. Hence, if the power stays self-averaged, the fluctuations will be as large as the signal itself. When we consider the transition from self-averaging to exponential decay, we consider only the statistics of the smoothed part of $P_{\rm ref}$, ignoring the oscillating part which does not contribute to the self-averaging. Thus in our theory we consider only the time-averaged power $\bar{P}_{\rm ref}(t)$, Eq. (2.26a), which is the key result of this section.

2.2 Finding $P_\gamma(\gamma_n)$

From Eq. (2.26a), we see that the average reflected power is a sum over contributions from exponentially decaying modes. Because of the exponential decay, the relative amplitudes of the modes will separate exponentially in time, with the modes with the smallest γ_n eventually dominating the sum. Thus, the crossover time from self-averaging to exponential decay depends on the behavior of the probability distribution function of γ_n for small values of γ_n. In this section we find the behavior of $P_\gamma(\gamma_n)$, the probability distribution function for the decay rates for $\gamma_n \ll \Delta\omega$. Previous work has been done on the subject (for instance, in the case of a lasing chaotic cavity, see Refs. [22, 48]), including analytical solutions for the $P_\gamma(\gamma)$ for all γ [24, 51], but because we focus on the single port case with time reversal symme-

try for small γ only, many approximations can be made which greatly simplify the derivation, which we present here.

We start by considering the statistics of ξ_n, where ξ_n is defined in Eq. (2.23). We show in Appendix A that the statistics of ξ_n are given in terms of the angle $\psi_n = \tan^{-1}(\xi_n)$, where ψ_n is distributed according to the pdf,

$$P_{\psi_n}(\psi_n) = \frac{\cos(\psi_n)}{2}. \tag{2.28}$$

Using this result and Eq. (2.21), we find an expression for $P_\gamma(\gamma_n)$ where $\gamma_n \ll \Delta\omega$:

$$P_\gamma(\gamma_n) = \frac{1}{\sqrt{2\pi}} \int_{-\pi/2}^{\pi/2} d\psi_n \, \cos\psi_n \int_0^\infty dw \, e^{-w^2/2} \delta\left(\gamma_n - w^2 \frac{r_r \Delta\omega}{\pi\left[1 + (r_r \tan(\psi_n) + x_{r,n})^2\right]}\right), \tag{2.29}$$

where $r_r = R_{Rad}(k)/Z_0$ and $x_r = X_{Rad}(k)/Z_0$. The innermost integral can be evaluated leaving only an integral over ψ_n. Further, since we are only interested in the case of small $\gamma_n \ll \Delta\omega$, the main contribution comes from $|w| \ll 1$. The result is

$$P_\gamma(\gamma_n) \cong \frac{P_0}{2\sqrt{\gamma_n \Delta\omega}} \text{ for } \gamma_n \ll \Delta\omega, \tag{2.30}$$

where

$$P_0 = (2r_r)^{-1/2} \int_{-\pi/2}^{\pi/2} d\psi_n \, \sqrt{\cos^2\psi_n + (r_r \sin\psi_n + x_r \cos\psi_n)^2}. \tag{2.31}$$

The quantity P_0 given in Eq. (2.31) can be rewritten in terms of the radiation reflection coefficient of the port that applies when the walls of the cavity have been moved out to infinity,

$$\rho_r = \frac{z_r - 1}{z_r + 1}, \tag{2.32}$$

where $z_r = r_r + ix_r = (R_{Rad} + jX_{Rad})/Z_0$ is the normalized radiation impedance of the antenna. To see this, we introduce the intermediate variable $\beta = z_r^2 - 1$ and define a new integration variable $\phi = \psi_n - \arg(\beta)/2$ in Eq. (2.31). The result of these variable changes is

$$P_0 = \sqrt{2\frac{1-|\rho_r|}{1+|\rho_r|}}E\left(\frac{2j\sqrt{|\rho_r|}}{1-|\rho_r|}\right), \tag{2.33}$$

where

$$E(k) = \int_0^{\pi/2} d\phi \sqrt{1-k^2\sin^2(\phi)} \tag{2.34}$$

is the complete elliptic integral of the second kind.

We confirm Eqs. (2.30) and (2.33) numerically by generating an ensemble of γ_n values. To do this we solve Eq. (2.15) by generating different realizations of the Gaussian random variables w_n and random matrix eigenvalues k_n^2 appearing in the definition of $Z(\omega)$, Eq. (2.10). We find the mode frequencies by noting that as $Z_0 \to \infty$, $\omega_n \to k_n c$ for all modes. We then introduce $Y_0 = Z_0^{-1}$ and differentiate both sides of Eq. (2.15) with respect to Y_0, obtaining a differential equation for $\omega_n(Y_0)$,

$$\frac{d\omega_n}{dY_0} = \frac{Z^2(\omega_n)}{Z'(\omega_n)}, \tag{2.35}$$

which can be solved numerically to find ω_n for finite Z_0. Note that although both $Z^2(\omega_n)$ and $Z'(\omega_n)$ are singular as $\omega_n \to k_n c$, their ratio is finite.

By generating 1000 different realizations of k_n^2 and ω_n (truncating the spectrum to include only 600 terms), and integrating Eq. (2.35) numerically using fourth-order Runga-Kutta from $Y_0 = 0$ to $Y_0 = R_{Rad}^{-1}$, it is possible to generate pdfs of $\tilde{w}_n \equiv \sqrt{\gamma_n}$ as a function of $|\rho_r|$. We choose the pdfs of $\tilde{w}_n$ instead of γ_n because

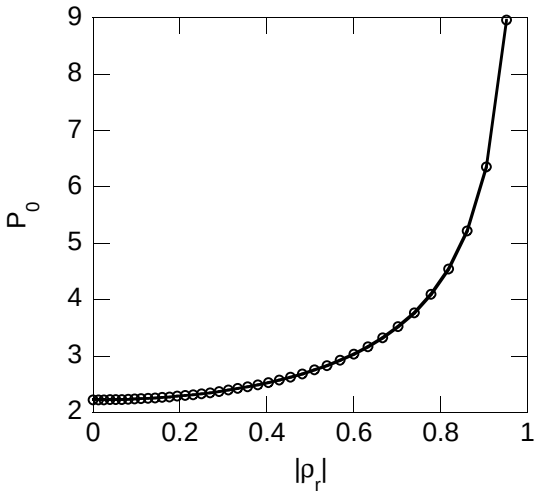

Figure 2.2: A comparison of numerically generated values for P_0 (circles) with the theoretical result from Eq. (2.33) (the solid line). The circles represent numerical calculations of P_0 with the radiation reactance of the port set to be $X_{Rad} = 0$. To get different values of $|\rho_r|$, Y_0 was changed as described in Eq. (2.35).

$P_{\tilde{w}}(\tilde{w} = 0) = P_0/\Delta\omega$, which is finite and thus numerically easier to fit. The results are shown in Fig. 2.2 where the numerical results and the theory are seen to be in clear agreement. We note that this numerical test (solving Eq. (2.35) for $Y_0 = R_{Rad}^{-1}$) does not assume the weak coupling limit and thus confirms our assumptions in obtaining Eq. (2.33).

2.3 The Statistics of $\bar{P}_{\rm ref}(t)$

The smoothed reflected power $\bar{P}_{\rm ref}(t)$ given by Eq. (2.26a) is a sum of terms each of which is a random variable. The terms are not strictly independent. This follow from the fact that there are correlations between the eigenvalues of the closed system, and γ_n, given by Eq. (2.21), depends on these eigenvalues through the reactance X_n, defined in Eq. (2.19). Fortunately the correlation is significant only

for almost adjacent modes. For times large enough that the self-averaging breaks, the fraction of modes contributing will be small, and thus, the majority of contributing modes will be well separated and approximately independent of each other.

Hence for our purposes, $\bar{P}_{\mathrm{ref}}$ can be treated as a sum of a large number of independent terms. Thus, for times when a large number (but small fraction) of modes have comparable magnitudes, for an ensemble of cavity realizations, $\bar{P}_{\mathrm{ref}}$ is a Gaussian random variable centered on $\langle \bar{P}_{\mathrm{ref}}(t) \rangle$ with a small standard deviation. As we demonstrate in the following sections, the standard deviation starts out small, but as the number of contributing modes decreases, the standard deviation increases relative to the mean, eventually becoming much larger than the mean. As this happens, the simple Gaussian distribution changes into a more complex distribution with the majority of modes becoming much smaller than the average, corresponding to the shift from self-averaging to exponential decay.

These shifts can be treated analytically by considering the moments of $\bar{P}_{\mathrm{ref}}$. We first (Sec. 2.3.1) consider the mean and standard deviation of $\bar{P}_{\mathrm{ref}}$ to find a scaling law describing the transition from Gaussian to non-Gaussian behavior. Armed with the results from this comparison, in Sec. 2.3.2 we generalize the results to higher-order moments (via the cumulants), showing that for large times all moments of $\bar{P}_{\mathrm{ref}}$ obey the same scaling law. We then numerically demonstrate that the cumulative distribution function of $\bar{P}_{\mathrm{ref}}/\langle \bar{P}_{\mathrm{ref}} \rangle$ satisfies the scaling law for multiple pulse shapes, as predicted.

2.3.1 The Mean and Variance

We can calculate the mean and the variance of $\bar{P}_{\rm ref}$ for all times as

$$\langle \bar{P}_{\rm ref} \rangle = \sum_n \frac{|2\pi\Delta\omega \bar{V}_{\rm inc}(\omega_n)|^2}{Z_0} \mu_1, \tag{2.36}$$

and

$$\langle (\bar{P}_{\rm ref} - \langle \bar{P}_{\rm ref} \rangle)^2 \rangle = \sum_n \frac{|2\pi\Delta\omega \bar{V}_{\rm inc}(\omega_n)|^4}{Z_0^2} (\mu_2 - \mu_1^2), \tag{2.37}$$

where

$$\mu_m(t) = \int_0^\infty \frac{d\gamma P_0}{2\sqrt{\gamma\Delta\omega}} \left[\frac{\gamma^2}{\Delta\omega^2} e^{-\gamma t} \right]^m. \tag{2.38}$$

Evaluation of the integral in Eq. (2.38) gives

$$\mu_m(t) = \frac{P_0}{2(m\Delta\omega t)^{2m+1/2}} \Gamma(2m + 1/2). \tag{2.39}$$

Equations (2.36) and (2.38) give the result that the average reflected power (averaged over an ensemble of reflecting cavities) decreases as a power law in time, which is in agreement with previous theory [17, 16],

$$\langle \bar{P}_{\rm ref}(t) \rangle \sim t^{-5/2}. \tag{2.40}$$

Equation (2.37) is useful for finding the range of values that are most likely to contain $\bar{P}_{\rm ref}$; for small times with an approximately Gaussian pdf for $\bar{P}_{\rm ref}$, we expect that the majority of realizations will fall within the range $[\langle \bar{P}_{\rm ref} \rangle - 2\sigma_P, \langle \bar{P}_{\rm ref} \rangle + 2\sigma_P]$ where $\sigma_P = \langle (\bar{P}_{\rm ref} - \langle \bar{P}_{\rm ref} \rangle)^2 \rangle^{1/2}$. For large times, however, $\sigma_P > \langle \bar{P}_{\rm ref} \rangle$. We see this by first considering the ratio

$$\frac{\mu_2}{\mu_1^2} = \frac{(\Delta\omega t)^{1/2}}{P_0} \frac{\Gamma(9/2)}{2^{7/2}\Gamma(5/2)^2}. \tag{2.41}$$

Thus, for large times, $\mu_2 \gg \mu_1^2$, and μ_2 dominates Eq. (2.37). For large times, we have

$$\frac{\sigma_P^2}{\langle \bar{P}_{\text{ref}} \rangle^2} = \frac{(t\Delta\omega)^{1/2}}{P_0} \frac{\Gamma(9/2)}{2^{7/2}\Gamma(5/2)^2} \frac{\sum_n |V_{\text{inc}}(\omega_n)|^4}{\left[\sum_n |V_{\text{inc}}(\omega_n)|^2\right]^2} \tag{2.42}$$

Equation (2.42) can be made more transparent by considering the sums over $|V_{\text{inc}}|^{2m}$. The incident pulse can be considered to have two independent properties: a shape and a width. If we double the width of the pulse in the frequency domain (or equivalently if we halve the average mode separation) without changing the shape, the sums in Eq. (2.42) will, to a good approximation, simply double. We thus define the effective number of modes excited by the wave to be

$$N = \frac{\left[\sum_n |V_{\text{inc}}(\omega_n)|^2\right]^2}{\sum_n |V_{\text{inc}}(\omega_n)|^4}. \tag{2.43}$$

In the case of a square wave excitation in the frequency domain, Eq. (2.43) gives exactly the number of modes excited. In the case of more typical pulses, such as a Gaussian pulse, Eq. (2.43) defines a relationship between the pulse width and the number of significant excited modes.

Substituting Eq. (2.43) into Eq. (2.42), we get

$$\frac{\sigma_P^2}{\langle \bar{P}_{\text{ref}} \rangle^2} = \tau^{1/2} \frac{\Gamma(9/2)}{2^{7/2}\Gamma(5/2)^2}, \tag{2.44}$$

where

$$\tau = \frac{t\Delta\omega}{N^2 P_0^2}. \tag{2.45}$$

As long as $\sigma_P / \langle \bar{P}_{\text{ref}} \rangle$ is small, it is reasonable to expect the majority of realizations of $\bar{P}_{\text{ref}}$ to be within two sigma of the average, and numerically we find that this is true. From Eq. (2.44), we see that for $t\Delta\omega \gg 1$ and $\tau \ll 1$ (possible because N

is assumed to be large) this is possible. Eventually the standard deviation will be comparable to the mean and for very long times the standard deviation will be much larger than the mean. This shift corresponds to the change from self-averaging to exponential decay.

2.3.2 Higher Moments

An analysis of the higher moments of $\bar{P}_{\text{ref}}$ follows essentially the same steps as those to find the mean and variance. We find the moments of $\bar{P}_{\text{ref}}$ by finding the moments of the individual terms in $\bar{P}_{\text{ref}}$, dropping all but the leading order term in $t^{-1/2}$, and combining them properly to get the moments of the sum. We cannot do this by simply summing the moments of the individual terms; the sums of the moments are not in general the moments of the sum. However, if we define the moment-generating function,

$$M(h) = \langle e^{h\bar{P}_{\text{ref}}} \rangle = 1 + \sum_{p=1}^{\infty} \frac{h^p \langle \bar{P}_{\text{ref}}^p \rangle}{p!}, \tag{2.46}$$

we see that the moments of $\bar{P}_{\text{ref}}$ are given by

$$\langle \bar{P}_{\text{ref}}^m \rangle = M^{(m)}(0). \tag{2.47}$$

Here $M^{(m)}(h)$ is the mth derivative of $M(h)$ with respect to its argument. This can be related to a function known as the cumulant-generating function

$$g(h) = \log(M(h)) = \sum_{p=1}^{\infty} \kappa_p \frac{h^p}{p!} \tag{2.48}$$

where κ_m is the mth cumulant, defined as

$$\kappa_m = g^{(m)}(0). \tag{2.49}$$

We show in Appendix (B) that, in analogy to Eq. (2.42), the higher-order cumulants (and thus all higher-order moments) of $\bar{P}_{\mathrm{ref}}$ are given by

$$\frac{\kappa_m}{\kappa_1^m} = \left(2\sqrt{\tau}\right)^{m-1} \frac{\Gamma(2m+1/2)}{m^{2m+1/2}\Gamma(5/2)^m} \frac{N^{m-1}\sum_n |V_{\mathrm{inc}}(\omega_n)|^{2m}}{\left(\sum_n |V_{\mathrm{inc}}(\omega_n)|^2\right)^m}. \tag{2.50}$$

If we use the definition of N from Eq. (2.43) and approximate all sums over n with integrals over ω_n, we find that the expression $N^{m-1}\sum_n |V_{\mathrm{inc}}(\omega_n)|^{2m} / \left(\sum_n |V_{\mathrm{inc}}(\omega_n)|^2\right)^m$ is, to a good approximation, independent of the width of the power spectrum but dependent on the shape. In the case of a square power spectrum, this factor is identically one for all m. For a Gaussian pulse we find that

$$\frac{N^{m-1}\sum_n |V_{\mathrm{inc}}(\omega_n)|^{2m}}{\left(\sum_n |V_{\mathrm{inc}}(\omega_n)|^2\right)^m} = \sqrt{\frac{2^{m-1}}{m}}. \tag{2.51}$$

Similarly, for a pulse with a Lorentzian power spectrum,

$$\frac{N^{m-1}\sum_n |V_{\mathrm{inc}}(\omega_n)|^{2m}}{\left(\sum_n |V_{\mathrm{inc}}(\omega_n)|^2\right)^m} = \frac{2^{m-1}\Gamma(m-\frac{1}{2})}{\sqrt{\pi}\Gamma(m)}. \tag{2.52}$$

Equation (2.50), combined with replacing the sums over $|V_{\mathrm{inc}}(\omega)|^{2m}$ with integrals, demonstrates the most important theoretical result of this chapter: *all statistical properties of the reflected power depend only on the shape of the pulse (independent of width) and the normalized time τ defined in Eq.* (2.45). Thus the cross-over from self-averaging to exponential decay, no matter how measured, will depend only on τ and the pulse shape.

2.4 Numerical Results

In this section, we compare different methods of calculating $\bar{P}_{\mathrm{ref}}(t)$ to show that our theoretical conclusions are correct. To view the resulting distributions,

we find the ensemble average of the calculated values of $\bar{P}_{\rm ref}(t)$ and then compare the individual realizations to the average. In particular, we define $C(\alpha, \tau)$ to be the fraction of realizations which are less than α times the ensemble average (i.e. $C(\alpha, \tau)$ is the cumulative distribution of $\bar{P}_{\rm ref}$ at the normalized time τ).

To both test and evaluate the theoretical results in Sec. 2.3, we perform two separate, independent calculations which should, according to our theory, produce the same results. The first method calculates the sum in Eq. (2.26a) with the γ_n independent of $\mathrm{Re}(\omega_n)$ and distributed according to the Porter-Thomas distribution with one degree of freedom,

$$P(\gamma) = \frac{e^{-\gamma/2}}{\sqrt{2\pi\gamma}}. \tag{2.53}$$

This distribution is chosen because it has the same behavior for small γ as is indicated in Eq. (2.30). We consider two different pulse spectra, $\bar{V}_{\rm inc}(\omega_n)$, Gaussian and Lorentzian, with two different widths $N = 20$ and 30, where N is defined in Eq. (2.43). Finally, we take the ω_n to be uniformly spaced when evaluating the sums. We call these results the theoretical results because they are a numerical evaluation of the theoretical assumptions used in Sec. 2.3. The theoretical results are shown in Fig. 2.3 for the case of the two pulse shapes and two spectral widths. The first thing to note about the plots is that the results for $N = 20$ and $N = 30$ lie on top of each other, showing that the definition of τ(Eq. 2.45) correctly accounts for variation of the pulse width. (There is a small deviation in the Lorentzian case for small values of α that will be addressed subsequently.) The second thing to note is that the $C(\alpha > 0.3)$ curves for the two pulse shapes are very similar. Thus, the

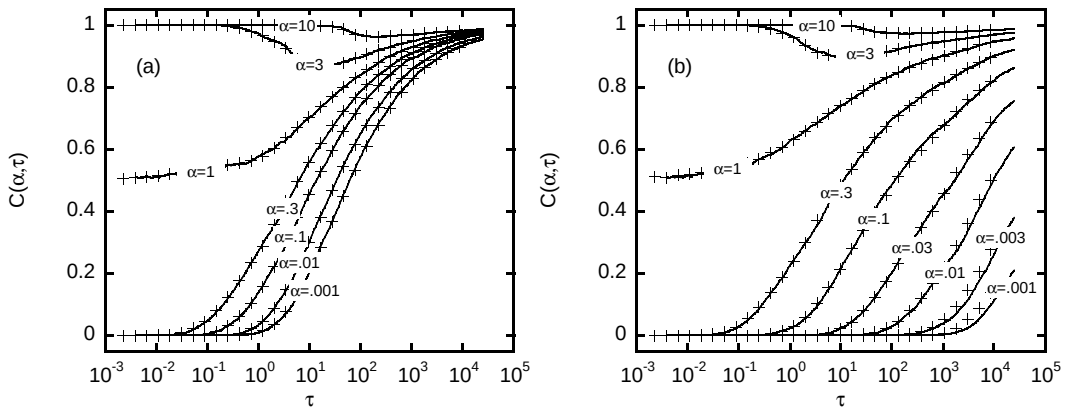

Figure 2.3: The fraction of realizations of $\bar{P}_{\rm ref}$ which are less than $\alpha\langle\bar{P}_{\rm ref}\rangle$ as a function of normalized time τ for (a) a Gaussian spectrum and (b) a Lorentzian spectrum. The black lines('+' symbols) represent the statistics for $N = 20(30)$. Note that plots for $N = 20$ and $N = 30$ are slightly different for the Lorentzian case with small α. This is due to the fact that the contributions for small α come from the tails of the distribution, which we numerically truncated to calculate these plots.

fraction of realizations close to or greater than the mean is the same in the two cases. Where the two pulse shapes differ is for times $\tau \gg 1$ and small $\alpha \ll 1$. In the Gaussian case almost all realizations fall well below the average as τ gets large, whereas in the Lorentzian case there is a larger fraction of realizations with measurable power ($\alpha > 0.001$) at late time. This is due to the long tail in the Lorentzian distribution exciting a large number of modes with small but significant levels of power. The difference between the $N = 20$ and $N = 30$ cases is due to truncation of the spectrum at 600 modes.

The second test employs the time-domain code used to generate the data in Fig. 2.1. We then time-smooth the resulting power (using a Gaussian window with a width of 10 Heisenberg times) to calculate $\bar{P}_{\rm ref}$. The time domain code is described in Appendix C. In Fig. (2.4) we compare results for $C(\alpha, \tau)$ using 50 realizations with

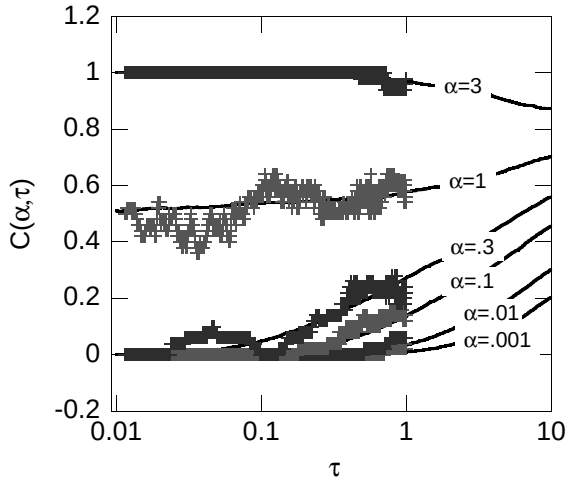

Figure 2.4: The fraction of realizations of $\bar{P}_{\rm ref}$ which are less than $\alpha\langle\bar{P}_{\rm ref}\rangle$ as a function of normalized time τ for the theoretical results calculated numerically (the solid lines) and the same results calculated from integrating Eq. (2.1) directly (indicated by the '+' symbols). Random Matrix Theory is explicitly used to calculate the spectrum and coupling constants for the time-domain integration.

the theoretical curves. The time-domain code is run only to $\tau = 1$ which for these parameters corresponds to 1744 Heisenberg times. The time domain simulation results agree well with the theoretical results considering the finite sample size.

In addition, we have performed tests which have allowed the value of P_0 to vary, and have solved Eq. (2.35) to get the complex values of ω_n. The results agree well with the theoretical results of Fig. 2.3 and are not displayed.

2.5 Conclusions

In this section, we have found numerically and theoretically that the long term behavior of power reflected from a lossless, microwave cavity excited through a single port self-averages for times larger than the Heisenberg time, decaying as a power law in time. We have also found, theoretically and numerically, that for times

much longer than the Heisenberg time, when τ, the normalized time, is of order 1, that single modes in the cavity will begin to dominate the long term decay and the reflected power will begin to decay exponentially. The details of this behavior have been found to depend on the shape of the power spectrum of the incident pulse that excited the cavity, but to otherwise depend only on the normalized time. Because much of the theory used to derive this behavior depends only on generic Random Matrix Theory, we expect that this behavior will translate into other lossless wave-chaotic systems (e.g., acoustic, quantum mechanical, etc.), independent of details.

Chapter 3

Refining the random coupling model: Short Bounce Orbits

3.1 Introduction

Wave systems appear in many different branches of physics, such as quantum mechanics, classical electromagnetism and acoustics. However, solving the wave equations in general can be quite difficult, particularly in the short wavelength limit for systems which have chaotic dynamics in the classical limit [31]. Furthermore, even if exact solutions were feasible, there may be uncertainties in the locations of boundaries or in parameters specifying the system. Thus, rather than solving such systems exactly, it has often been convenient to create statistical models which reproduce the generic properties of such systems without the need to accurately model the details [32]. One successful statistical approach, known as random matrix theory, is to replace the exact wave-mechanical operators, such as the Hamiltonian or scattering matrix, with matrices whose elements are assumed to be random. Although such formulations cannot predict any particular wave system's properties exactly, they can predict the distribution of properties in an ensemble of related wave-chaotic systems. Random matrix theory also predicts the statistical properties of a *single* wave-chaotic system evaluated at different frequencies. The random matrix technique applies to a wide range of systems and has been well studied both theoretically and experimentally. See Refs. [2, 29, 27, 5] for reviews of the theory,

history and applications of random matrix theory.

In this chapter, we use random matrix theory to model the scattering behavior of an ensemble of wave-chaotic systems coupled to the outside world through M discrete scattering channels. Such scattering systems have been studied extensively, with most work focusing on the $M \times M$ scattering matrix $\boldsymbol{S}$, either by using a random Hamiltonian for the closed system and deriving the resulting scattering matrix using assumptions for the coupling between the wave system and the scattering channels [9] or by replacing the scattering matrix with a random matrix directly [19, 18, 43, 41, 42]. These two approaches are complementary and for some ensembles have been explicitly shown to be equivalent [9].

We consider ensembles of systems whose distribution of scattering matrices are well-described by the so-called Poisson kernel [19, 43, 18]. The Poisson kernel characterizes the probability density for observing a particular scattering matrix $\boldsymbol{S}$ in terms of the average scattering matrix $\bar{\boldsymbol{S}}$, which is also called the 'optical scattering matrix'. It represents contributions to the scattering matrix from elements of the system which are not random. For instance, if the scattering channels are not perfectly coupled to the wave system, some fraction of the energy in the incident waves will simply bounce off the interface between the channel and the scatterer without experiencing the chaotic aspects of the scatterer, thus strongly constraining $\bar{\boldsymbol{S}}$. This is known as the prompt reflection [1]. In addition, rays within the scatter-

[1]In nuclear scattering, the scattering dynamics naturally splits into two different timescales, with reflections due to poor coupling and so-called "direct processes" occurring very quickly compared to the slow "equilibrated response." In these cases, the direct processes are usually included

ing region which connect the scattering channels without ergodically exploring the chaotic dynamics also affect $\bar{\boldsymbol{S}}$ [41, 11].

Because $\bar{\boldsymbol{S}}$ is the only parameter in the Poisson kernel, methods of finding it for a specific system are of interest. Although $\bar{\boldsymbol{S}}$ can be extracted quite simply from experimental data, *predicting* it from first principles is quite difficult in general, although it has been done for for some specific systems such as quantum graphs [38]. In most wave systems, however, it depends in a complicated way on the interactions between the scattering channels, the wave system, and any significant classical trajectories. To address this problem, we find it convenient to transform from the scattering matrix $\boldsymbol{S}$ to the $M \times M$ impedance matrix $\boldsymbol{Z}$ [58, 59, 60],

$$\boldsymbol{Z} = \boldsymbol{Z}_0^{1/2}(\mathbf{1} + \boldsymbol{S})(\mathbf{1} - \boldsymbol{S})^{-1}\boldsymbol{Z}_0^{1/2}. \tag{3.1}$$

where $\boldsymbol{Z}_0$ is an $M \times M$ diagonal matrix whose ith diagonal element is determined by the detailed properties of the ith scattering channel as described below. We will show that the average impedance matrix (to be defined) can be expressed directly in terms of classical ray trajectories.

Impedance is a meaningful concept for all scattering wave systems. In linear

in the term "prompt reflection." In microwave billiards, the distinction between direct processes and equilibrated response is much less clear because the relevant time-scales are not nearly as well separated. However, in microwave billiards, the size of the ports used to couple into the system are typically much smaller than any of the other distances in the system and therefore respond much more quickly to incident waves. Thus we designate only the reflections due to the dynamics within the ports as the prompt response.

electromagnetic systems, it is defined via the phasor generalization of Ohm's law as

$$\hat{V} = \boldsymbol{Z}\hat{I}, \tag{3.2}$$

where the M-dimensional vector $\hat{\boldsymbol{V}}$ represents the voltage differences across the attached transmission lines (the systems port) and the M-dimensional vector $\hat{\boldsymbol{I}}$ denotes the currents flowing through the transmission lines. The concept of impedance can be generalized to cases where the cavity is excited through apertures connected to waveguides that may support several propagating modes. In acoustics, the impedance is the ratio of the sound pressure to the fluid velocity. A quantum-mechanical quantity corresponding to impedance is the reaction matrix, which is often denoted in the literature as $i\boldsymbol{K}$ [2].

The diagonal elements of $\boldsymbol{Z}_0$ are the characteristic impedances of the scattering channels. In electromagnetic systems with transmission lines for scattering channels, the characteristic impedances are the ratio between the voltage difference across the transmission line and the current through the transmission line for a monochromatic wave propagating a single direction through the transmission line. Other wave systems have analogous definitions for $\boldsymbol{Z}_0$ determined by the details of the scattering channels. In what follows, we use terminology appropriate in the context of an electromagnetic cavity connected to the outside world via transmission line channels.

With the transformation to impedance, we find that we can define an "average" impedance matrix $\boldsymbol{Z}_{avg}$ which is related to $\bar{\boldsymbol{S}}$ via the transformation,

$$\boldsymbol{Z}_{avg} = \boldsymbol{Z}_0^{1/2}(\mathbf{1} + \bar{\boldsymbol{S}})(\mathbf{1} - \bar{\boldsymbol{S}})^{-1}\boldsymbol{Z}_0^{1/2}. \tag{3.3}$$

In contrast to $\bar{\boldsymbol{S}}$, we find that $\boldsymbol{Z}_{avg}$ can be evaluated directly in the semiclassical

limit as a sum over contributions from the prompt reflection and short classical trajectories. Thus, through (3.3) this gives a method for approximating $\bar{\boldsymbol{S}}$ in the semiclassical limit.

In this chapter, we present our approach to calculating $\boldsymbol{Z}_{avg}$. In Sec. 3.2, we provide an overview of our theory for lossless systems and describe the most important results of our investigations. In Sec. 3.3, we find expressions for the impedance of a specific quasi-2D lossless microwave cavity as explicit functions of the boundaries and port positions, creating a framework in which we can keep some cavity properties fixed and let others change. We then apply the semiclassical approximation to our exact formulations. In Sec. 3.3.1, we use the semiclassical approximation to derive expressions for the impedance induced by objects near the port in terms of classical short orbits between the ports and the internal scatterers. In Sec. 3.3.2, we use the semiclassical approximation to convert our exact solution with integral operators into a finite-dimensional matrix equation with an internal scattering matrix $\boldsymbol{T}$. In Sec. 3.4, we assume that the matrix $\boldsymbol{T}$ is distributed according to the Poisson kernel with the average $\boldsymbol{T}$ given by the results of Sec. 3.3 and use a result by Brouwer [9] to find the corresponding distribution for the impedance. In Sec. 3.5, we demonstrate that in the lossless case, our theory agrees with numerical simulations of our system. In Sec. 3.6, we extend our theory to lossy cavities and briefly refer to experimental results in lossy systems which will be published separately.

3.2 Overview of Lossless Theory

The results presented in this chapter are an extension of our previously developed random coupling model [59, 60, 58]. For simplicity, we consider only systems and frequencies in which the scattering channels have a single propagating mode and in which the ports which couple the scattering channels to the cavity are separated from each other by much more than a wavelength. We found previously with these assumptions that by replacing the resonant frequencies of our closed chaotic cavity with a set of resonant frequencies appropriate to a random matrix drawn from the Gaussian orthogonal ensemble and modeling the eigenfunctions using the random-plane wave hypothesis, the impedance of our lossless wave-chaotic systems could be described by [60]

$$\boldsymbol{Z} = i\boldsymbol{X}_R + i\sqrt{\boldsymbol{R}_R}\boldsymbol{\xi}_0\sqrt{\boldsymbol{R}_R}, \tag{3.4}$$

where $\boldsymbol{R}_R$, the radiation resistance, and $\boldsymbol{X}_R$, the radiation reactance, are the real and imaginary parts of the $M \times M$ diagonal radiation impedance matrix $\boldsymbol{Z}_R$, which represents the impedance the scattering system would have if all the energy which successfully coupled into the system was absorbed rather than allowed to couple back out. The matrix $\boldsymbol{\xi}_0$ is an element of the appropriate $M \times M$ Lorentzian ensemble introduced by Brouwer [9] with width 1 and median 0, which in the single-port case simplifies to a Lorentzian random variable with width 1 and median 0. We denote $\boldsymbol{\xi}_0$ the normalized impedance and have previously studied its properties in chaotic systems [58, 59, 60, 36].

Equation (3.4) is the direct impedance analog of the Poisson kernel distri-

bution for $\boldsymbol{S}$ in the case that the only contribution to $\bar{\boldsymbol{S}}$ is due to the 'prompt reflections' caused by the impedance mismatch between the scattering channels and the wave system [58]. From experimental measurements and simulation results performed using the commercial off-the shelf program High Frequency Structure Simulator(HFSS), we know that Eq. (3.4) describes the impedance statistics of our sample systems only if the impedances are sampled from a very wide frequency range [58]. We find, however, that if we consider sample impedances from either narrower frequency ranges or from many slightly different chaotic systems, the distribution of the resulting impedances is still well-described by a Lorentzian distribution, but with a different median and width than that predicted by Eq. (3.4).

These deviations are illustrated in Fig. 3.1, which shows the median calculated impedance for the quasi-two dimensional cavity illustrated in Fig. 3.2 (its dimensions are given in Sec. 3.5). This cavity was the basis for our previous numerical and experimental research. It is a simulated electromagnetic cavity filled with a uniform lossless dielectric and is coupled to the outside world through coaxial cables (the ports) inserted into holes on the top of the cavity. For the data in Fig. 3.1, only port 1 is present. On the walls we impose perfect-conductor boundary conditions. Because our cavity has a uniform height h in the z-direction which is much smaller than the wavelength of the incident microwaves, Maxwell's equations become effectively two-dimensional with the electric and magnetic fields uniform in the z-direction [52, 59]. This system is an example of a wave billiard, meaning that the rays within the cavity follow straight lines except for specular reflection at the walls. To produce the simulation data shown in Fig. 3.1, we generated 95 different realizations of

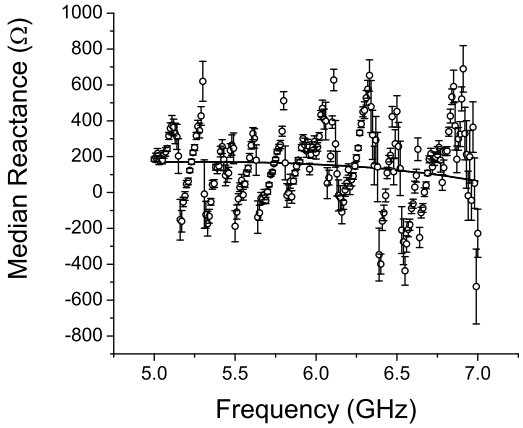

Figure 3.1: A comparison between the port radiation reactance as measured by HFSS (solid line) and the ensemble median of the HFSS simulated impedances (circles). The random coupling model predicts that if the ensemble is sufficiently random, the ensemble median should equal the radiation reactance. The error bars were estimated by assuming that the ensemble impedance is a Lorentzian random variable (justified by statistical examination of the ensemble data) and finding the uncertainty in the median, given the numerically found width. The differences between these two curves are caused by short orbits within the cavity which exist in many realizations of the ensemble.

related systems by adding a small mobile perturber to our baseline system and moving it to 95 different, widely-spaced locations (see Fig. 3.2). We then find that, at each frequency, the distribution of impedances is Lorentzian, but with a median and width which are different from $\boldsymbol{X}_R$ and $\boldsymbol{R}_R$. (For this example, $\boldsymbol{X}_R$ and $\boldsymbol{R}_R$ are scalars.) We also find that as a function of frequency, the fitted medians and widths oscillate almost symmetrically around $\boldsymbol{X}_R$ and $\boldsymbol{R}_R$. As we will later see, this behavior arises because short classical trajectories within the system alter the distribution of impedances, analogous to the distortion of $\bar{\boldsymbol{S}}$ observed in previous work [41, 42, 11].

In this chapter, we show that corrections to the radiation impedance matrix due to the direct orbits redefine $\boldsymbol{Z}_R$ in an additive way, $\boldsymbol{Z}_R \rightarrow \boldsymbol{Z}_{avg} = \boldsymbol{Z}_R +$ [direct orbit terms]. More specifically, we find that

$$\boldsymbol{Z}_{avg} = \boldsymbol{Z}_R + \boldsymbol{R}_R^{1/2} \boldsymbol{\zeta} \boldsymbol{R}_R^{1/2}, \tag{3.5}$$

where $\boldsymbol{\zeta}$ is an $M \times M$ dimensionless matrix whose (m, n)th element describes the effects of wave propagation from port m to port n and is explicitly defined in Eq. (3.50). The individual elements $\zeta_{m,n}$ are each a sum over all different possible ray paths going from port m to port n, with each path having a phase factor proportional to the length of the path and prefactors describing the directivity of the classical trajectories relative to the shape of the ports, the stability of the ray trajectory and the number of reflections from the boundaries. In addition, in cases where the geometry of the cavity is varied to create an ensemble (for example by moving a perturber throughout the cavity) there is a factor that accounts for the fraction of realizations in which that particular path will contribute (i.e., not be blocked by the perturber). We note that as the frequency window within which sample impedances are generated gets wider and/or the ensemble changes more drastically between realizations, the value of $\boldsymbol{\zeta}$ needed to normalize the data goes to 0 and we get our original random coupling model back as a limit.

The substitution of $\boldsymbol{Z}_{avg}$ for $\boldsymbol{Z}_R$ can be understood to be a generalization of the radiation impedance of the ports to include the effects of features of the cavity that are distant from the ports but that do not vary from one member of the ensemble to another. Consider an ensemble of lossless microwave cavities whose

generic properties (such as volume and circumference) are fixed but whose shapes are random and independent *except* that the ports are always placed in the same positions relative each other and except that some segments of the wall are also fixed. The impedance of each configuration will reflect the interaction between the ports and both the fixed and varying segments at the wall. The interactions between the ports and fixed wall segments will be the same for each member of the ensemble and will contribute to the average impedance while the interactions between the ports and the varying segments will vary from member to member and contribute to statistical deviations from the average. As our subsequent analysis will show, the ports and fixed wall segments can together be considered to be a single super-port which has a radiation impedance of $\boldsymbol{Z}_{avg}$, thus justifying replacing $\boldsymbol{Z}_R$ with $\boldsymbol{Z}_{avg}$ in Eq. (3.4).

3.3 The Impedance as a Function of Cavity Shape

For the electromagnetic system described in Sec. 3.2, we previously derived [60] the following inhomogeneous wave equation for the case where the ports are modeled by vertical (z-direction), externally imposed, localized current densities flowing from the bottom to the top plates,

$$\left(\nabla_\perp^2 + k^2\right) \hat{V}_T(\vec{r}) = ikh\eta \sum_{p=1}^{M} u_p(\vec{r}) I_p, \tag{3.6}$$

where $\nabla_\perp$ is the 2D Laplacian in the (x, y) plane,$\hat{V}_T$ represents the voltage difference between the two plates, I_p represents the total current injected into the cavity through port p, $u(\vec{r})$ represents the profile of the current injected onto the top plate

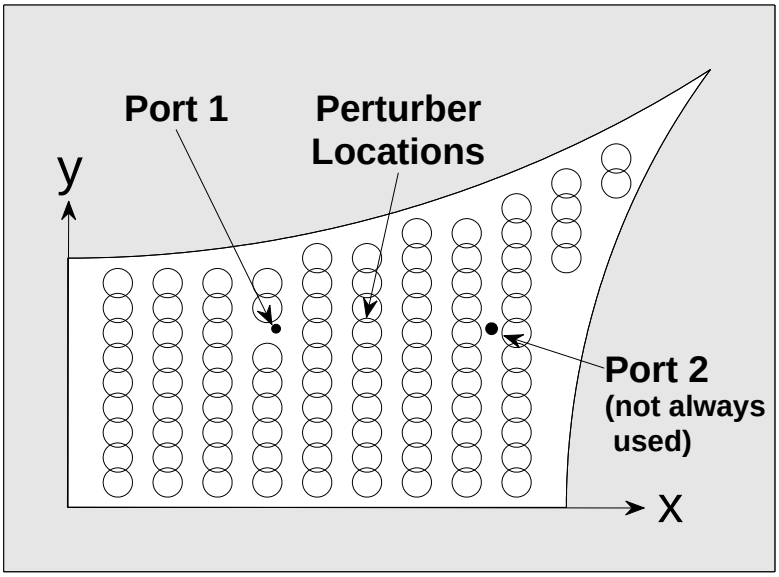

Figure 3.2: This plot displays a 2-D view of our simulated microwave cavity and the perturber positions used to produce the ensemble displayed in Fig. 3.1. The outer walls are fixed in all realizations, while every realization has the perturber at a different location. The microwaves are fed into the cavity through the ports, which are coaxial cables inserted through the top of the cavity. The dimension h of the cavity in the z-direction (out of the page) are much smaller than the wavelengths used to excite the cavity and therefore results in effectively two-dimensional waves in the x-y plane.

at port p and has the property $\int d\vec{r}'\, u(\vec{r}') = 1$, $\eta = \sqrt{\mu/\epsilon}$ is the wave impedance of propagation within the medium inside the cavity (i.e. η is the ratio of the electric field to the magnetic field in an infinite plane wave), and $k = 2\pi/\lambda$ is the wave-number of the external driving frequency. With perfect-conducting boundary conditions, V_T must be zero on the cavity boundary. The model of the port considered here is appropriate to the case in which the port is smaller than a wavelength so that the distribution of current (given by $u(\vec{r}')$) is fixed, independent of frequency of the fields in the cavity $V_T(\vec{r})$. In this way each port is characterized by a single current I_p, and a corresponding voltage [60],

$$V_p = \int d^2\vec{r}'\, u_p(\vec{r}')V_T(\vec{r}'). \tag{3.7}$$

Definition (3.7) was selected in Ref. [59] since it yields $P = (1/2)\mathrm{Re}\{V_p^* I_p\}$ for the power flow into the cavity. The cavity impedance then gives the matrix relation between the port currents I_p and port voltages V_p.

Equation (3.6) is the driven Helmholtz equation, and although it was derived in the context of quasi-2D electromagnetic cavities and a particular port model, it can be applied to many different types of systems (such as quantum dots or acoustic resonators) simply by relabeling the constants and tweaking the boundary conditions [52].

Before considering statistics, we first derive an expression for the impedance for individual realizations of the cavity. Similar to previous work by Georgeot and Prange [25], we can convert Eq. (3.6) into an integral equation. We do this by

introducing the outgoing Green's function $G_0(\vec{r}, \vec{r}'; k)$ which satisfies

$$\left(\nabla_\perp^2 + k^2\right) G_0(\vec{r}, \vec{r}'; k) = \delta(\vec{r} - \vec{r}'). \tag{3.8}$$

We then multiply both sides of Eq. (3.6) by $G_0(\vec{r}, \vec{r}'; k)$ and integrate both sides over $\vec{r}'$ obtaining

$$\int_{\mathcal{D}} d^2\vec{r}' G_0(\vec{r}, \vec{r}') \left(\nabla_\perp'^2 + k^2\right) \hat{V}_T(\vec{r}') = ikh\eta \sum_{p=1}^{M} I_p \int_{\mathcal{D}} d^2\vec{r}' G_0(\vec{r}, \vec{r}') u_p(\vec{r}'), \tag{3.9}$$

where $\mathcal{D}$ denotes the two-dimensional domain within the cavity. Applying Green's second identity in two dimensions to the left-hand side of Eq. (3.9) and applying the boundary condition on $\hat{V}(\vec{r})$, this becomes

$$\hat{V}_T(\vec{r}) = -\int_{\partial\mathcal{D}} dq'\, G_0(\vec{r}, q') \frac{\partial \hat{V}_T(q')}{\partial n'} + ikh\eta \sum_{p=1}^{M} I_p \int_{\mathcal{D}} d^2\vec{r}' G_0(\vec{r}, \vec{r}') u_p(\vec{r}') \tag{3.10}$$

where q' represents a position on the boundary $\partial\mathcal{D}$ of the cavity and the integral over q' integrates over the cavity boundary $\partial\mathcal{D}$, and where $\partial/\partial n'$ denotes a derivative in the direction normal to the surface of the cavity at q'.

In electromagnetic systems, Eq. (3.10) has a physical interpretation. From Maxwell's equations and the perfect conductor boundary conditions, we find that the gradient of the voltage, $\vec{\nabla}\hat{V}_T$ is proportional to the surface current in the upper and lower plate of the cavity, with the two currents flowing in opposite directions. At the edges of the cavity, the surface current flowing in the lower plate travels up the outer wall and into the top plate. Thus it temporarily travels in the z-direction. We can then interpret Eq. (3.10) as stating that the electric field inside the cavity is simply the sum over the field radiating from the changing currents in the ports and the field radiating from the changing current in the outer walls. Therefore, solving

Eq. (3.10) is equivalent to finding the self-consistent current induced in the walls, given the currents in the ports. We evaluate the normal derivative of Eq. (3.10) on the surface to get our integral equation,

$$\frac{\partial \hat{V}_T(q)}{\partial n} = -\int_{\partial\mathcal{D}} dq' \, \frac{\partial G_0(q,q')}{\partial n} \frac{\partial \hat{V}_T(q')}{\partial n'} + ikh\eta \sum_{p=1}^{M} I_p \int_{\mathcal{D}} d^2\vec{r}' \frac{\partial G_0(\vec{r},\vec{r}')}{\partial n} u_p(\vec{r}'). \quad (3.11)$$

We henceforth drop the subscripts $\partial\mathcal{D}$ and $\mathcal{D}$ on the integral symbols. As long as the function defining the boundary of the cavity is well-behaved, Eq. (3.11) is a Fredholm integral equation of the second type and can be solved via the established Fredholm theory [53].

To simply and clarify our results, we follow Prange, Fishman and Georgeot [25, 21], and define the operators

$$\begin{aligned}
\boldsymbol{K}\phi(q) &= -\int dq' \, \frac{\partial G_0(q,q')}{\partial n}\phi(q'), \\
\boldsymbol{V}_+ u(\vec{r}) &= \frac{1}{\sqrt{k}} \int d^2\vec{r}' \, \frac{\partial G_0(q,\vec{r}')}{\partial n} u(\vec{r}'), \\
\boldsymbol{V}_- \phi(q) &= \sqrt{k} \int dq' \, G_0(r,q')\phi(q'), \\
\boldsymbol{G_0} u(\vec{r}) &= \int d^2\vec{r}' \, G_0(\vec{r},\vec{r}')u(\vec{r}').
\end{aligned} \quad (3.12)$$

In these operators, q and q' are real scalars denoting points on the cavity boundary $\partial\mathcal{D}$. They represent distance along the boundary of the cavity as measured relative to some arbitrary starting position. The vectors $\vec{r}$ and $\vec{r}'$ represent positions within the cavity (i.e. within $\mathcal{D}$). Every operator integrates over a primed variable and maps it onto the space represented by the unprimed variable.

These operators all have physical meanings in electromagnetism. G_0 is the two-dimensional, outgoing Green's function in empty space; it finds the voltage at

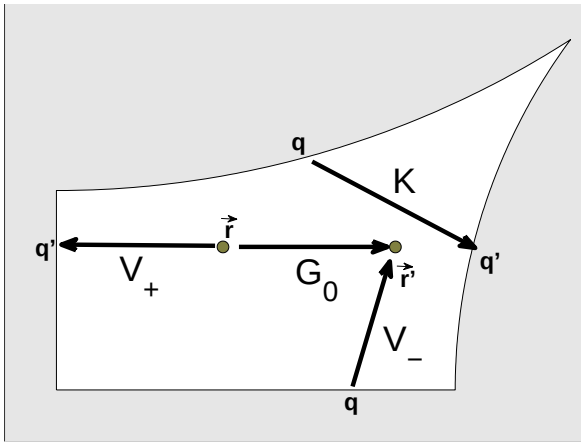

Figure 3.3: A schematic of the different operators defined in Eq. (3.12). Each operator takes a current at the source position and finds the resulting current ($\boldsymbol{K}$ and $\boldsymbol{V}_+$) or voltage ($\boldsymbol{G}_0$ and $\boldsymbol{V}_-$) induced at the endpoint.

some position $\vec{r}$ caused by a delta-function current distribution at point $\vec{r}'$. The operator $\boldsymbol{V}_+$ finds the current induced in the wall by a delta-function current in the volume. The operator $\boldsymbol{K}$ represents the current induced in one part of the wall by the current in another part of the wall. The operator $\boldsymbol{V}_-$, on the other hand, gives the voltage inside the volume which results from the currents in the walls. A schematic of the effects of these operators is shown in Fig. 3.3.

Using this operator notation and solving Eq. (3.11), we convert Eq. (3.10) into

$$\hat{V}_T(\vec{r}) = ikh\eta \sum_{p=1}^{M} I_p \left[\boldsymbol{V}_- \left(\mathbf{1} - \boldsymbol{K}\right)^{-1} \boldsymbol{V}_+ + \boldsymbol{G_0}\right] u_p(\vec{r}). \tag{3.13}$$

In Fredholm theory, the operator $\left(\mathbf{1} - \boldsymbol{K}\right)^{-1}$ is well-defined and can be defined as a ratio of two convergent sums

$$\left(\mathbf{1} - \boldsymbol{K}\right)^{-1} = \frac{\sum_{n=0}^{\infty} \sum_{r=0}^{n} \boldsymbol{K}^{n-r} d_r}{\sum_{n=0}^{\infty} d_n}, \tag{3.14}$$

where d_n is an nth order polynomial in the traces of $\boldsymbol{K}^m$, $m \leq n$. For more details on constructing d_n, see the references [25, 21], where it is denoted D_n.

Using the definition of port voltage, Eq. (3.7), we get the impedance between ports n and m

$$Z_{n,m} = ikh\eta \int d^2\vec{r}\, u_n(\vec{r}) \left[\boldsymbol{V}_- \left(\mathbf{1} - \boldsymbol{K} \right)^{-1} \boldsymbol{V}_+ + \boldsymbol{G_0} \right] u_m(\vec{r}). \tag{3.15}$$

The second term in the integral on the right-hand side of Eq. (3.15) represents the impedance the system would have if the walls were moved to infinity and outgoing boundary conditions were imposed but impedance due to direct orbits between the ports were still included. Therefore, we define an $M \times M$ matrix $\tilde{\boldsymbol{Z}}_{\boldsymbol{R}}$ which has the elements

$$\tilde{Z}_{R,n,m} = ikh\eta \int d^2\vec{r}\, u_n(\vec{r}) \boldsymbol{G_0} u_m(\vec{r}). \tag{3.16}$$

The diagonal elements of $\tilde{\boldsymbol{Z}}_R$ are equal to the diagonal elements of the radiation impedance $\boldsymbol{Z}_R$ from Eq. (3.4) [59] and the off-diagonal elements represent contributions to the impedance from direct orbits between the ports. Because the distance between the ports is large compared to a wavelength, we can treat the off-diagonal terms semiclassically. The diagonal terms $\tilde{Z}_{R,n,n}$ depend on near-field interactions within the port and thus are sensitive to the detailed properties of the port. As in Eq. (3.4), rather than attempting to solve the for the diagonal elements of $\tilde{\boldsymbol{Z}}_R$, we treat them as inputs to the theory. This has the advantage of freeing us from a detailed port model; we expect our model to be accurate even when the port behavior is not modeled by Eq. (3.6).

In addition, we define the corresponding radiation resistance and radiation

reactance matrices as

$$\tilde{\boldsymbol{R}}_R = \frac{1}{2}\left(\tilde{\boldsymbol{Z}}_R + \tilde{\boldsymbol{Z}}_R^\dagger\right), \tag{3.17}$$

$$\tilde{\boldsymbol{X}}_R = -\frac{i}{2}\left(\tilde{\boldsymbol{Z}}_R - \tilde{\boldsymbol{Z}}_R^\dagger\right), \tag{3.18}$$

where † denotes the conjugate transpose. In the case of the Helmholtz equation, or any system in which time-reversal symmetry is present, $\tilde{\boldsymbol{Z}}_R$ is symmetric and so $\tilde{\boldsymbol{R}}_R$ and $\tilde{\boldsymbol{X}}_R$ are simply the real and imaginary components of $\tilde{\boldsymbol{Z}}_R$.

Equation (3.15) is an exact solution to Eq. (3.6) explicitly in terms of the boundaries. Analytically it is intractable. In the following two sections, we consider two different, but equivalent, approximations to Eq. (3.15). It is by equating these two different formalisms that we derive our refined theory.

3.3.1 The short-orbit formulation

To get useful theoretical results from Eq. (3.15), we make the assumption that each port p is located near the position $\vec{r}_{0,p}$ and that $u(\vec{r})$ is nonzero only within a small radius around $\vec{r}_{0,p}$. We assume that the ports are physically separated from each other and from the walls by much more than a wavelength, and that the dimensions of the cavity as a whole are much larger than a wavelength. With these assumptions, we find that all integrals in Eq. (3.15) (except the diagonal terms in Eq. (3.16)) evaluate G_0 or its derivatives in the far-field limit. Thus, we approximate G_0 and its derivatives with their asymptotic forms, which replaces $\boldsymbol{K}$ with Bogomolny's transfer operator $\boldsymbol{T}$ [8], which in the electromagnetic case is given

by

$$T(q,q';k) = \frac{-i}{4}\sqrt{D_{\vec{r},\vec{r}'}}e^{iS(\vec{r},\vec{r}';k)-i\pi/4}\sqrt{\frac{\cos(\theta_f)}{\cos(\theta_i)}}, \tag{3.19}$$

where $\theta_i(\theta_f)$ is the angle between the initial(final) wave vector and the surface at the position it leaves(hits), $S(\vec{r},\vec{r}';k)$ is the classical action along the direct trajectory from $\vec{r}$ to $\vec{r}'$, and $\sqrt{D_{\vec{r},\vec{r}'}}$ is the stability of the orbit from $\vec{r}$ to $\vec{r}'$, defined formally as

$$D_{\vec{r},\vec{r}'} = \frac{2}{\pi k^2}\left|\frac{\partial^2 S(\vec{r},\vec{r}')}{\partial \vec{r}_\perp \partial \vec{r}'_\perp}\right|, \tag{3.20}$$

where the derivative with respect to $\vec{r}_\perp(\vec{r}'_\perp)$ denotes the gradient with respect to $\vec{r}(\vec{r}')$ dotted into a unit vector perpendicular to the initial(final) momentum of the classical trajectory from $\vec{r}$ to $\vec{r}'$.

We note that the approximation made in Eq. (3.19) can be used to extend our theory beyond Eq. (3.6) by simply changing $\boldsymbol{T}$ to represent the semiclassical approximation for other physical situations. For instance, it is possible to allow $\boldsymbol{T}$ to have a different action depending on the direction of travel, thus violating time-reversal symmetry. It is also possible to add loss or gain to the system by adding a complex component to the action.

With these assumptions and approximations, we find

$$\boldsymbol{G_0}u_p(\vec{r}') \approx \frac{-i\pi}{2k}\sqrt{D_{\vec{r},\vec{r}'}}e^{iS(\vec{r},\vec{r}_{0,p})-i\pi/4}\tilde{u}_p(-\vec{k}_i(\vec{r},\vec{r}')), \tag{3.21}$$

where we have expanded $S(\vec{r},\vec{r}') \approx S(\vec{r},\vec{r}_{0,p}) - \vec{k}_i(\vec{r},\vec{r}_{0,p})\cdot\Delta\vec{r}$, the quantity $\vec{k}_i(\vec{r},\vec{r}')$ is the initial wave vector for the classical trajectory from $\vec{r}$ to $\vec{r}'$, and $\tilde{u}_p(\vec{k})$ is the Fourier transform of $u_p(\vec{r})$ centered on $\vec{r}_{0,p}$:

$$\tilde{u}_p(\vec{k}) = \int d^2\Delta\vec{r}\, e^{i\vec{k}\cdot\Delta\vec{r}}u_p(\vec{r}_{0,p}+\Delta\vec{r}). \tag{3.22}$$

If we insert Eq. (3.14) into Eq. (3.15), we find

$$Z_{n,m} = Z_{R,n,m} + \frac{ikh\eta \sum_{n=0}^{\infty} \sum_{r=0}^{n} d_r \int d^2\vec{r}\, u_n(\vec{r}) \boldsymbol{V}_- \boldsymbol{K}^{n-r} \boldsymbol{V}_+ u_m(\vec{r})}{\sum_{n=0}^{\infty} d_n}. \tag{3.23}$$

Thus the impedance depends only on d_n, which depends on $\mathrm{Tr}(\boldsymbol{K}^n)$, and on integrals over the operators $\boldsymbol{V}_-\boldsymbol{K}^{n-r}\boldsymbol{V}_+$. Evaluating all integrals using stationary phase, the prefactors and wave vectors are selected such that [31, 8]

$$\int d^2\vec{r}\, u_n(\vec{r}) \boldsymbol{V}_- \boldsymbol{K}^{l-1} \boldsymbol{V}_+ u_m(\vec{r}) = \sum_{b(l,m,n)} \frac{\tilde{u}_n(\vec{k}_f)\tilde{u}_m^*(\vec{k}_i)}{4} \sqrt{D_{b(l,m,n)}} e^{iS_{b(l,m,n)} - i\pi/4}, \tag{3.24}$$

where $b(l,m,n)$ is an index over all classical trajectories that bounce l times, starting at the center of port m and ending at the center of port n, $S_{b(l,m,n)}$ is the action for the corresponding classical trajectory and $D_{b(l,m,n)}$ is the stability coefficient defined as in Eq. (3.20) with $S(\vec{r},\vec{r}') \to S_{b(l,m,n)}$.

At this point we bring attention to the fact that the boundary of the cavity does not need to be connected. For example, in the cavity of Fig. 3.2 there is a circular perturber that is moved about, creating an ensemble of different cavities. That circle represents a portion of the boundary that is not connected to the outer portion of the cavity boundary. Equation (3.24) in principle includes trajectories that pass through the perturber in going from one point on the surface to another. (In addition Eq. (3.24) includes trajectories that can pass through the convex upper boundary of Fig. 3.2.) However, Bogolmony considered such trajectories [8] and found that such unphysical orbit terms come in pairs whose semiclassical contributions cancel exactly. Thus, the sum over all semiclassical bounce terms, which is all that we will consider, will include only physical contributions.

It was found in previous work [59] that the radiation resistance for our model ports is given by

$$R_{R,p}(k) = \frac{kh\eta}{4} \int \frac{d\theta}{2\pi} |\tilde{u}_p(k\hat{\theta})|^2, \tag{3.25}$$

where $\hat{\theta}$ is the two-dimensional unit vector $(\cos(\theta), \sin(\theta))$, which when inserted into Eq. (3.24) gives

$$kh\eta \int d^2\vec{r}\, u_n(\vec{r}) \boldsymbol{V}_- \boldsymbol{K}^{l-1} \boldsymbol{V}_+ u_m(\vec{r}) = \sqrt{R_{R,n} R_{R,m}} \sum_{b(l,m,n)} C_{b(l,m,n)} e^{iS_{b(l,m,n)} - i\pi/4}, \tag{3.26}$$

where

$$C_{b(l,m,n)} = \frac{u_n(\vec{k}_f) u_m^*(\vec{k}_i)}{\sqrt{\langle |u_n|^2 \rangle \langle |u_m|^2 \rangle}} \sqrt{D_{b(l,m,n)}}. \tag{3.27}$$

Using similar logic, we can also calculate the off-diagonal terms of Eq. (3.16),

$$Z_{R,n,m} = \sqrt{R_{R,n} R_{R,m}} C_{(0,m,n)} e^{iS_{(0,m,n)} - i\pi/4}, n \neq m, \tag{3.28}$$

where $C_{(0,m,n)}$ and $S_{(0,m,n)}$ are the corresponding prefactor and action for a direct orbit from port m to port n. We view the sum over $b(l, m, n)$ as adding successively longer length orbits, and we thus refer to Eqs. (3.25)-(3.28) as the 'short orbit formalism'.

With this result and similar semiclassical results for $\mathrm{Tr}(\boldsymbol{K}^l)$ [26], it is possible in principle to evaluate Eq. (3.15) semiclassically for any cavity. We will not need to perform this entire calculation explicitly, however. Instead, we will use the results from the next section to relate the sums over classical trajectories to the elements of random matrices.

We test this short-orbit formalism using the HFSS program. In the simulator, we construct a fully three-dimensional cavity and antenna system similar to the

one used in previous research; the quasi-2D nature of the cavity is enforced by choosing the excitation frequency to be below the cut-off frequency for modes that vary between the top and bottom plates.

To test our short-orbit theory, we first simulate the radiation impedance of a single cylindrically-symmetric antenna by placing the antenna inside a circular cavity, where the outer circular wall has absorbing boundary conditions (to simulate the radiation condition of purely outgoing waves) and the port was off-center (this was to reduce coherent numerical reflections from the outer wall; the numerical absorbing boundary condition is imperfect). As expected, we find a slowly varying function of frequency for both the radiation resistance R_R and reactance X_R. We then change the cavity by introducing one perfectly conducting wall into the system, effectively producing a cavity in which all waves would either radiate away or bounce once off the single wall and then radiate away, thus isolating a single term in Eq. (3.26). Plots of such isolated bounce terms are shown in Figs. 3.4-3.6.

We find empirically that each short orbit term experiences a frequency-dependent phase shift $\Delta\phi_p$ when coupling through the port p, requiring the introduction of a phase factor $e^{i(\Delta\phi_n+\Delta\phi_m)}$ to Eq. (3.26). Although this phase shift is frequency dependent, in the cylindrically symmetric case it is orbit-independent; thus it is possible to measure the phase shift using one short orbit and then apply it to all others. For our ports, it is most convenient to introduce this phase shift and the cylindrical symmetry by simply setting

$$C_{b(l,m,n)} = e^{i(\Delta\phi_n+\Delta\phi_m)}\sqrt{D_{b(l,m,n)}}. \tag{3.29}$$

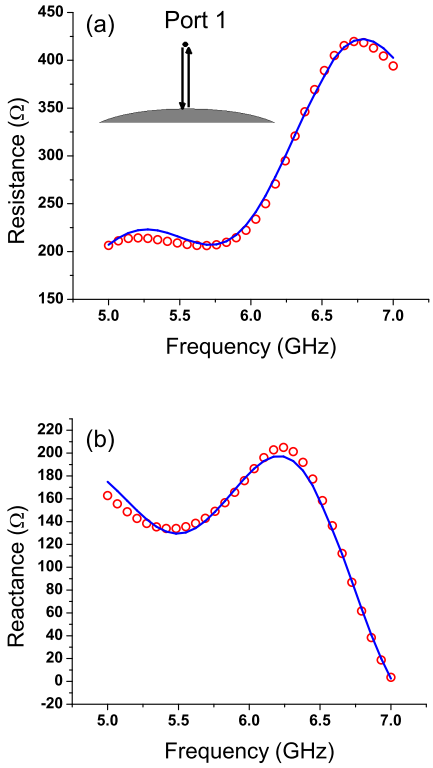

Figure 3.4: Comparison of the simulated impedance (circles) and theoretical impedance (solid line) of a single port with a circular perfectly conducting scatterer on one side and radiation boundary conditions on all other sides (see the inset in plot a). The radius of curvature of the scatterer is 1.02 meters and its surface is 7.6 centimeters from the port. The radiation impedance and phase shift for the port were extracted from independent simulation data. Plot (a) shows the resulting resistances and plot (b) shows the reactances. (Color online)

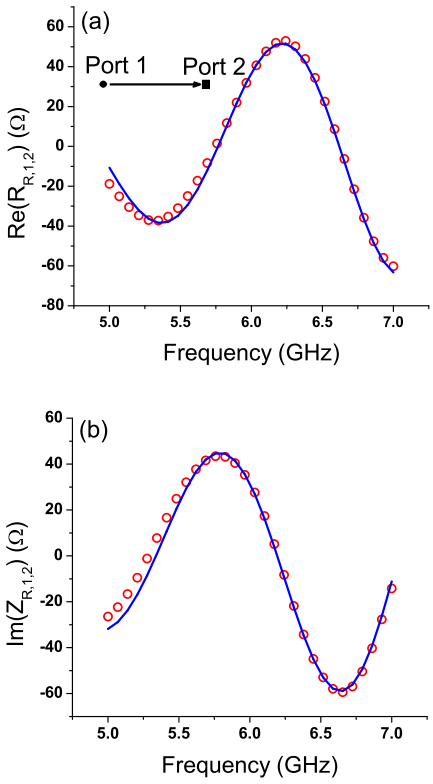

Figure 3.5: Comparison of the simulated (circles) and theoretical (solid line) $Z_{R,1,2}$ when the ports are separated by a distance of 14.4 centimeters. Note that unlike the diagonal impedance matrix elements, the real part of the off-diagonal terms can be negative. The radiation impedances and phase shifts were extracted from independent simulations of each port. (Color online)

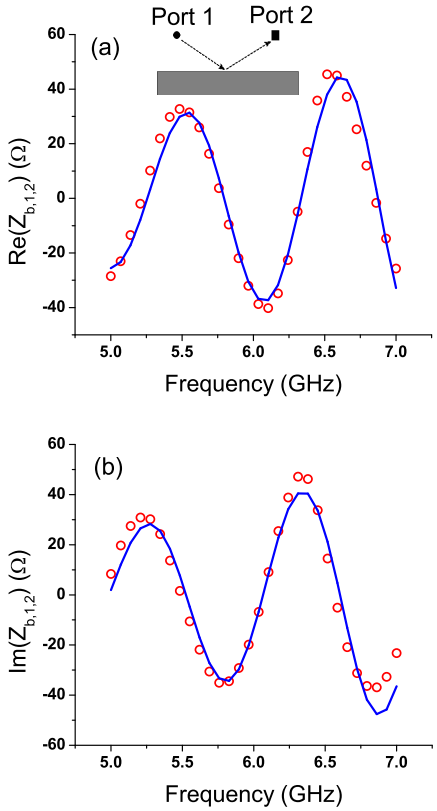

Figure 3.6: Comparison of the simulated (circles) and theoretical (solid line) impedance due to the orbit shown in the inset in (a). The ports were 14.4 centimeters apart and 10 centimeters from the reflecting wall. This impedance is found by finding the total impedance of the system with the reflecting wall nearby and radiation boundary conditions everywhere else and then subtracting the radiation impedance as found in Fig. 3.5. We denote it $Z_{b,1,2}$. The radiation impedances and phase shifts were extracted for each port from independent simulation data. (Color online)

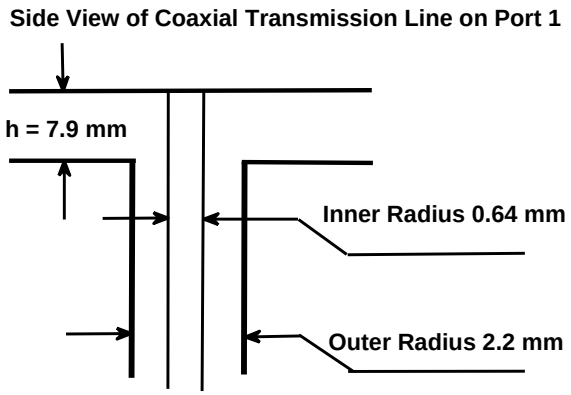

Figure 3.7: Cross-section of the port connecting transmission line 1 and the microwave cavity.

This phase shift exists due to the fact that in the HFSS simulations, we model the ports in detail as a circular cross-section coaxial transmission line in which the outer conductor contacts the upper plate and the inner conductor extends the short way across the cavity and contacts the lower plate. The shape and dimensions of port 1 are shown in Fig. 3.7. Port 2, when it is present, has the same geometry as port 1, but with an outer radius of 3.0 mm. This more detailed port model results in an additional phase shift that is not treated in our simple model of Eq. (3.6) where we add a fixed current source to the wave equation. With this phase correction in $C_{b(l,m,n)}$, however, we find that we can model the impedance very well by using Eq. (3.26).

To show the agreement between theory and simulation, we create three different cavity configurations. In the first configuration, we have a single port with a single conducting, curved wall near it, with absorbing boundary conditions on the

remaining surfaces. After simulating the isolated ports radiation impedance and finding the phase shift, we both predict and simulate the resulting impedance in the presence of the curved wall. Fig. 3.4 shows the measured and the predicted impedance from 5 to 7 GHz, both resistance and reactance, where it can be seen that the theoretical and simulated results agree well. The deviations between the two are expected; the semiclassical approximation is not perfect at frequencies this low, and we also have diffraction from the necessary truncation of the wall.

In the second configuration, we tested Eq. (3.24) by introducing a second antenna into the system and imposing radiation boundary conditions on all the outer walls. We found the radiation impedance and phase shift of the second antenna using exactly the same methods as for the first. We then simulated the mutual impedance between the two ports and compared it to Eq. (3.28) using the simulated port parameters, and found that the agreement was again excellent, as shown in Fig 3.5.

The third configuration is the same as the second, except we add a conducting wall next to the two ports, creating an orbit which leaves the first port, bounces off the wall once, and goes to the second port. To isolate the impedance due to this new orbit, we compare the changes in impedance (which we denote $Z_{b,1,2}$) between configurations 2 and 3 rather than the raw impedances. Comparing this difference with the semiclassical prediction from Eq. (3.26), we again see excellent agreement, as shown in Fig. 3.6.

Thus we believe that our short-orbit formulation is effective at predicting the impedance of cavities with a few, short orbits. In the next section, we discuss

an equivalent formulation which expresses the impedance as elements of a finite-dimensional matrix. This equivalence between the matrix and semiclassical formulations will allow us to create ensembles of cavities which account for short orbits within the cavity.

3.3.2 The finite matrix formulation

The results of Sec. 3.3.1 are based on an evaluation of the continuous, integral operator $\boldsymbol{K}$ defined in Eq. (3.12). To make connection with random matrix theory, we wish to recast the equations in matrix form. The authors of Ref. [21] have shown how to do this. Further, in the semiclassical limit, the resulting matrix is effectively finite.

To derive the matrix formulation, we first replace the continuous operator $\boldsymbol{K}$ with the semiclassical operator $\boldsymbol{T}$. Then we use the result that semiclassically [21],

$$i\boldsymbol{V}_{-}\boldsymbol{T}^{\dagger} = \boldsymbol{V}_{+}{}^{\dagger}. \tag{3.30}$$

The operator $\boldsymbol{V}_{+}{}^{\dagger}\boldsymbol{V}_{+}$ was also found in the semiclassical approximation to be [21]

$$\boldsymbol{V}_{+}{}^{\dagger}\boldsymbol{V}_{+} = i\left(\boldsymbol{G_0} - \boldsymbol{G_0}^{\dagger}\right). \tag{3.31}$$

By using Eq. (3.30) to eliminate $\boldsymbol{V}_{-}$ and by adding $\left[\boldsymbol{V}_{+}{}^{\dagger}\boldsymbol{V}_{+} - i\left(\boldsymbol{G_0} - \boldsymbol{G_0}^{\dagger}\right)\right]/2$, which is zero, to the operator inside Eq. (3.15), we can rewrite the impedance as

$$\begin{aligned} Z_{n,m} &= \frac{1}{2}kh\eta \int d^2\vec{r}\, u_n(\vec{r}) \left[\boldsymbol{V}_{+}{}^{\dagger}\frac{\mathbf{1}+\boldsymbol{T}}{\mathbf{1}-\boldsymbol{T}}\boldsymbol{V}_{+} + i\left(\boldsymbol{G_0} + \boldsymbol{G_0}^{\dagger}\right)\right] u_m(\vec{r}), \\ &= iX_{R,n,m} + \frac{1}{2}kh\eta \int d^2\vec{r}\, u_n(\vec{r})\boldsymbol{V}_{+}{}^{\dagger}\frac{\mathbf{1}+\boldsymbol{T}}{\mathbf{1}-\boldsymbol{T}}\boldsymbol{V}_{+}u_m(\vec{r}). \end{aligned} \tag{3.32}$$

Fishman, Prange and Georgeot [21] demonstrated that in the semiclassical limit, the operator $\boldsymbol{T}$ can be represented as an infinite-dimensional matrix whose components are zero except on a finite subspace of dimension $N = 2L/\lambda$, where in our formulation L is the circumference of the cavity. They demonstrated this by expanding all functions on their surface of section (in our formulation, the cavity boundary) in a Fourier series. In this basis, an arbitrary function $\nu(q)$ is expanded as

$$\nu(q) = \sum_{n=-\infty}^{\infty} a_n e^{2\pi niq/L}. \tag{3.33}$$

They showed that the operator $\boldsymbol{T}$, evaluated using stationary phase in this basis, is insensitive to Fourier components smaller than a wavelength, resulting in the truncated subspace. By identical logic, the operator $\boldsymbol{V}_+$ only projects onto this semiclassical subspace. Thus, semiclassically, the function $\boldsymbol{V}_+ u_p(\vec{r})$ is non-zero only on this subspace, where it has N discrete components corresponding to the Fourier components of the expansion in Eq. (3.33).

Using Eq. (3.31), we get the dot product between two of these vectors,

$$\begin{aligned} \int d^2\vec{r}\, u_n(\vec{r}) \boldsymbol{V}_+{}^\dagger \boldsymbol{V}_+ u_m(\vec{r}) &= i \int d^2\vec{r}\, u_n(\vec{r}) \left(\boldsymbol{G_0} - \boldsymbol{G_0}^\dagger\right) u_m(\vec{r}) \\ &= \frac{2\tilde{R}_{R,n,m}}{kh\eta}. \end{aligned} \tag{3.34}$$

Thus we can rewrite Eq. (3.32) as

$$\boldsymbol{Z} = i\tilde{\boldsymbol{X}}_R + \boldsymbol{v}^\dagger \cdot \frac{\mathbf{1} + \boldsymbol{T}}{\mathbf{1} - \boldsymbol{T}} \cdot \boldsymbol{v} \tag{3.35}$$

where we now treat $\boldsymbol{T}$ as an $N \times N$ matrix and where $\boldsymbol{v}$ is an $N \times M$ matrix whose columns $\vec{v}_p$ are the N-dimensional vectors proportional to the semiclassical $\boldsymbol{V}_+ u_p(\vec{r})$

and which are normalized such that

$$\boldsymbol{v}^{\dagger}\boldsymbol{v} = \tilde{\boldsymbol{R}}_R. \tag{3.36}$$

Because Eqs. (3.26), (3.28) and (3.36) are all evaluated in the stationary phase approximation, we can equate the matrix elements of any power of $\boldsymbol{T}$ with the semiclassical orbit terms

$$2\vec{v}_n^{\dagger} \cdot \boldsymbol{T}^{l-1} \cdot \vec{v}_m = \sqrt{R_{R,n}R_{R,m}} \sum_{b(l,m,n)} C_{b(l,m,n)} e^{iS_{b(l,m,n)} - i\pi/4}. \tag{3.37}$$

Equation (3.37) is one of the most important results of this chapter. By explicitly connecting the semiclassical sums to a semiclassical matrix formulation of impedance, we can relate the classical trajectories to the more abstract operator formalism. Thus when we create ensembles of $\boldsymbol{v}$ and $\boldsymbol{T}$, we can relate the ensemble averages of $\boldsymbol{v}$ and $\boldsymbol{T}$ to the corresponding ensemble averages of the classical trajectories within the cavity, which gives us a natural method of creating ensembles of $\boldsymbol{T}$ which are constrained by short orbits within the system.

3.4 Impedance Statistics

As noted in the introduction, it is often difficult to solve the wave equation exactly. Even in the semiclassical regime, where the problem is in principle tractable using classical trajectories, there are difficulties. If the classical dynamics is chaotic, the number of classical trajectories grows exponentially as does their sensitivity to numerical errors. Small mistakes in modeling or small changes between similar systems will result in large changes in the observed behavior. Thus we follow the

long-standing tradition of replacing our deterministic expressions with statistical models which reproduce the generic behavior of the systems being considered.

Our model for the cavity impedance is given in Eq. (3.35). The matrices $\tilde{\boldsymbol{X}}_R$ and $\boldsymbol{v}$ (up to an unmeasurable and thus arbitrary basis, which can thus be absorbed into $\boldsymbol{T}$) are determined by Eqs. (3.16) and (3.17), which depend only on the radiation fields from the ports, and are thus amenable to direct measurement or non-chaotic semiclassical theory. Thus to find our statistical properties, we simply seek an appropriate distribution for $\boldsymbol{T}$.

The matrix $\boldsymbol{T}$ may be viewed as representing an internal scattering matrix. In the case of chaotic dynamics and in the context of random matrix theory, it is most natural to model $\boldsymbol{T}$ as an element of Dyson's circular ensemble [19] (with the time-reversal symmetry determined by the symmetry of the underlying system). If we make this substitution, it can be shown that the resulting statistical properties of $\boldsymbol{Z}$ are completely equivalent to our previously published random coupling model. In this model, the system specific properties of the ports (specifically the radiation impedance) are all that is used to "normalize" the statistically fluctuating impedance. Effectively, the previous model assumes that once wave energy enters the cavity it is randomized by the chaotic ray trajectories such that no details of the interior of the cavity modify the statistics of the impedance. However, we have seen in Fig. 3.1 that there is likely some influence of specific ray trajectories within the cavity on the statistical properties (in the case of Fig. 3.1 the median) of the impedance. We now assume that the effect of these trajectories can described by the Poisson kernel [43]. That is, we assume that the distribution of $\boldsymbol{T}$ is given by

the Poisson kernel [41]

$$P(\boldsymbol{T}) = \frac{1}{2^{N(\beta N+2-\beta)/2}V} \frac{\det\left(\mathbf{1} - \bar{\boldsymbol{T}}^\dagger \bar{\boldsymbol{T}}\right)^{(\beta N+2-\beta)/2}}{\det\left(\mathbf{1} - \bar{\boldsymbol{T}}^\dagger \boldsymbol{T}\right)^{\beta N+2-\beta}} \tag{3.38}$$

where V is a normalization constant and $\bar{\boldsymbol{T}}$ is the average value of $\boldsymbol{T}$ over the ensemble, and $\bar{\boldsymbol{T}}$ is, in principle, determined explicitly by the boundaries of the cavities in the ensemble.

The Poisson kernel does not just specify the average value of $\boldsymbol{T}$; it has the general property that [43]

$$\langle \boldsymbol{T}^l \rangle = \bar{\boldsymbol{T}}^l. \tag{3.39}$$

If we knew $\bar{\boldsymbol{T}}$, then we could find the distribution of $\boldsymbol{Z}$ directly. Unfortunately, finding $\bar{\boldsymbol{T}}$ for a specific ensemble such as that shown in Fig. 3.2 is almost as complex as finding $\boldsymbol{T}$ and thus has no advantage over numerically solving the Helmholtz equation. By averaging both sides of Eq. (3.37), however, we can find the components of $\bar{\boldsymbol{T}}^l$ spanned by the column vectors of $\boldsymbol{v}$. We find that knowing these average short orbit terms for all l is sufficient to get the statistics of $\boldsymbol{Z}$; because the sum over average short orbits is expected to converge, the problem becomes tractable for a wide range of ensembles.

With this assumption for the distribution of $\boldsymbol{T}$, we can find the statistical properties of $\boldsymbol{Z}$. From a result due to Brouwer for matrices distributed according to the Poisson kernel [9], we find that we can parameterize $\boldsymbol{T}$ as

$$\boldsymbol{T} = \frac{i\boldsymbol{W}^\dagger\left(\lambda\tilde{\boldsymbol{H}}_{\mathbf{0}} + \epsilon\mathbf{1}\right)\boldsymbol{W} - \mathbf{1}}{i\boldsymbol{W}^\dagger\left(\lambda\tilde{\boldsymbol{H}}_{\mathbf{0}} + \epsilon\mathbf{1}\right)\boldsymbol{W} + \mathbf{1}}, \tag{3.40}$$

where the scalars λ, ϵ and the $N \times N$ matrix $\boldsymbol{W}$ are ensemble-specific constants

which depend only on $\bar{\boldsymbol{T}}$, and $\tilde{\boldsymbol{H}}_{\boldsymbol{0}}$ is an $N \times N$ random matrix distributed according to the pdf of the Lorentzian ensemble with median 0 and width 1,

$$P(\tilde{\boldsymbol{H}}_{\boldsymbol{0}}) = \frac{1}{V} \frac{\lambda^{N(\beta N+2-\beta)/2}}{\det(\mathbf{1} + \tilde{\boldsymbol{H}}^2)^{(\beta N+2-\beta)/2}}, \tag{3.41}$$

where $\beta = 1(2, 4)$ for the Orthogonal(Unitary,Symplectic) choice of time-reversal behavior. Inserting Eq. (3.40) into Eq. (3.35), we find

$$\boldsymbol{Z} = i\tilde{\boldsymbol{X}}_R + i\lambda(\boldsymbol{W}\boldsymbol{v})^\dagger \tilde{\boldsymbol{H}}_0 \boldsymbol{W}\boldsymbol{v} + i\epsilon(\boldsymbol{W}\boldsymbol{v})^\dagger \boldsymbol{W}\boldsymbol{v}. \tag{3.42}$$

We now wish to eliminate λ, ϵ and $\boldsymbol{W}\boldsymbol{v}$ from Eq. (3.42). We do this by noting that given the parametrization in Eq. (3.40), Brouwer found the value of $\bar{\boldsymbol{T}}$ to be [9]

$$\bar{\boldsymbol{T}} = \frac{(\lambda + i\epsilon)\boldsymbol{W}^\dagger \boldsymbol{W} - \mathbf{1}}{(\lambda + i\epsilon)\boldsymbol{W}^\dagger \boldsymbol{W} + \mathbf{1}}. \tag{3.43}$$

Solving Eq. (3.43) for $\boldsymbol{W}^\dagger \boldsymbol{W}$ and projecting both sides onto the subspace spanned by $\boldsymbol{v}$, we get

$$(\lambda + i\epsilon)\,(\boldsymbol{W}\boldsymbol{v})^\dagger \cdot (\boldsymbol{W}\boldsymbol{v}) = \boldsymbol{Z}_{avg} - i\tilde{\boldsymbol{X}}_R, \tag{3.44}$$

where we formally define $\boldsymbol{Z}_{avg}$ as

$$\boldsymbol{Z}_{avg} = i\tilde{\boldsymbol{X}}_R + \boldsymbol{v}^\dagger \cdot \frac{\mathbf{1} + \bar{\boldsymbol{T}}}{\mathbf{1} - \bar{\boldsymbol{T}}} \cdot \boldsymbol{v}. \tag{3.45}$$

We denote the Hermitian and anti-Hermitian components of $\boldsymbol{Z}_{avg}$ as $\boldsymbol{R}_{avg}$ and $\boldsymbol{X}_{avg}$, respectively. Matching the Hermitian and anti-Hermitian components across the equality in Eq. (3.44) and noting that $\boldsymbol{R}_{avg}$ must be a non-negative matrix because $\bar{\boldsymbol{T}}$ is subunitary and normal, we find that

$$\lambda\,(\boldsymbol{W}\boldsymbol{v})^\dagger\,\boldsymbol{W}\boldsymbol{v} \;=\; \boldsymbol{R}_{avg} \tag{3.46}$$

$$\epsilon\,(\boldsymbol{W}\boldsymbol{v})^\dagger\,\boldsymbol{W}\boldsymbol{v} \;=\; \boldsymbol{X}_{avg} - \tilde{\boldsymbol{X}}_R. \tag{3.47}$$

Inserting these results into Eq. (3.42) gives us

$$\boldsymbol{Z} = i\boldsymbol{X}_{avg} + i\sqrt{\boldsymbol{R}_{avg}}\boldsymbol{\xi}\sqrt{\boldsymbol{R}_{avg}} \tag{3.48}$$

where $\boldsymbol{\xi}$ is $\tilde{\boldsymbol{H}}_0$ projected onto the subspace spanned by $\boldsymbol{W}\boldsymbol{v}$. Brouwer proved that any diagonal submatrix of a Lorentzian distributed matrix is also a Lorentzian distributed matrix with the same median and width. This result combined with the basis invariance of Eq. (3.41) leads to the conclusion that $\boldsymbol{\xi}$ is a Lorentzian random matrix with width 1 and median 0, as predicted. The basis-invariance of the distribution of $\tilde{\boldsymbol{H}}_0$ also means that although Eq. (3.46) has a family of related solutions for $\boldsymbol{W}\boldsymbol{v}$, all members of this family are related via a change of basis and therefore result in identical statistics for $\boldsymbol{Z}$.

Although knowing the form of the distribution for $\boldsymbol{Z}$ is useful and can be used fruitfully to fit experimental or simulation data, at a single frequency it is only a minor improvement over the Poisson kernel in which one can also extract $\bar{\boldsymbol{S}}$ from numerical data [41, 42]. Our last step is therefore to predict the value of $\boldsymbol{Z}_{avg}$ using the semiclassical approximations developed in Sec. 3.3.1. We do this by noting that because $\bar{\boldsymbol{T}}$ is subunitary, the magnitude of all its eigenvalues are less than or equal to one. The set of $\bar{\boldsymbol{T}}$ which have any eigenvalues on the unit circle has measure zero. Therefore we can expand Eq. (3.45) in a convergent series as

$$\boldsymbol{Z}_{avg} = \tilde{\boldsymbol{Z}}_R + 2\sum_{l=1}^{\infty} \boldsymbol{v}^\dagger \cdot \bar{\boldsymbol{T}}^l \cdot \boldsymbol{v}. \tag{3.49}$$

Substituting Eqs. (3.37) and (3.28) into Eq. (3.49), and remembering Eq. (3.39), we see that semiclassically $\boldsymbol{Z}_{avg}$ is the port impedance plus the sum of the average contributions the short orbits make to the impedance. In our case, where we have a

perturber which moves much more than a wavelength between realizations through the entire cavity, the contributions of orbits reflected off the perturber will have an essentially random phase, and we approximate their contributions as zero. Because the outer walls are fixed, short orbits from the ports to the walls will systematically appear in the sum in Eq. (3.49), but must be weighted by p_b, the fraction of realizations in which they do not pass through the perturber. With these results, we find the elements of $\boldsymbol{\zeta}$ from Eq. (3.5) to be

$$\zeta_{n,m} = \sum_{b(n,m)} p_{b(n,m)} C_{b(n,m)} e^{iS_{b(n,m)}(k) - i\pi/4} \tag{3.50}$$

where the index $b(n,m)$ is over all short orbits which go from port m to port n, including direct orbits between different ports. Note that when we test this theory, we use the empirically discovered form of $C_{b(n,m)}$ from Eq. (3.29).

We note that $\boldsymbol{Z}_{avg}$ is the impedance the baseline system would have if some fraction of energy were lost every time a wave passed through a perturber. Even for very large numbers of bounces, this seems to be a general result: the impedance needed to normalize the statistics of any sufficiently random ensemble will correspond to the impedance of a single lossy cavity where loss occurs in those features which change between realizations, with the degree of loss determined by the degree of change in those elements. Thus even with very small perturbations in which the semiclassical approach is unfeasible, the form of $\boldsymbol{Z}_{avg}$ is known, and in analogy to the Poisson kernel, we can fit to find the effective radiation impedance. More importantly this implies that the frequency dependence of $\boldsymbol{Z}_{avg}$ matches that of an appropriate lossy cavity. If the perturbations are sufficiently uniform within the cav-

ity, the statistics of $\boldsymbol{Z}_{avg}$ evaluated over a range of sufficiently separate frequencies would exhibit the statistics found in our previous work for lossy cavities.

In microwave billiards exhibiting hard chaos with a uniform distribution of perturber locations within the volume, it is possible to estimate the expected loss parameter for $\boldsymbol{Z}_{avg}$. Because typical ray trajectories within the cavity explore the phase space ergodically and because the perturber locations are distributed uniformly, we expect that, $p_{b(n,m)} \sim \exp(-\tilde{\alpha} L_{b(n,m)})$, where $\tilde{\alpha}$ is determined by the perturber size and shape and the perturber locations, and $L_{b(n,m)}$ is the length of the $b(n,m)$th orbit. Neglecting the phase shifts from the traversals of the ports (which are expected to be small due to the small size of the ports), we find that with this expression for $p_{b(n,m)}$,

$$\zeta_{n,m} \sim \sum_{b(n,m)} C_{b(n,m)} \exp(i(k + i\tilde{\alpha}) L_{b(n,m)} - i\pi/4), \tag{3.51}$$

where we have used that the classical action in microwave billiards is given by $S_{b(n,m)} = kL_{b(n,m)}$. We found in previous work [59] that the transformation $k \rightarrow k + i\tilde{\alpha}$ corresponds to adding loss, with the loss parameter given by $Q = k/(2\tilde{\alpha})$ and the line-width to level spacing ratio $\alpha = kA\tilde{\alpha}/\pi$, where A is the area of the microwave cavity. Thus, by analogy, introducing p_b into Eq. (3.50) is roughly equivalent to $\boldsymbol{Z}_{avg}$ being the impedance of a lossy cavity with uniform loss. Using a Monte Carlo simulation of long ray trajectories in our bowtie billiard, we find that for the perturber positions in Fig. 3.2, $\tilde{\alpha} \sim .25m^{-1}$.

This result for the average impedance is related to work done by Brouwer and Beenakker [10] following Büttiker [12]. In their work, they found that a lossy quan-

tum dot could be modeled as a lossless quantum dot coupled both to the physical scattering channels and to a large number of weakly coupled parasitic channels. Because $\boldsymbol{Z}_{avg}$ represents the impedance of a system where a small amount of energy is lost when it passes through a perturber position, the perturber positions function as effective parasitic channels, and we expect the resulting average impedance and average scattering matrix to be well-fit by their theory.

3.5 Numerical Tests of the Theoretical Predictions

In this section, we show the results of several tests of Eqs. (3.5) and (3.50) for both one and two-port configurations. We obtained the data for these tests from simulations using HFSS. The cavity configuration we used is shown in Fig. 3.2. Port 1 is centered at location (x = 18.03cm, y = 15.48cm) and port 2 (when it is present) is at (x = 36.7cm,y = 15.48cm). The lower-left corner of the cavity is at (x = 0.0cm, y = 0.0cm). Both ports have essentially the geometry as shown in Fig. 1 of Reference [59], but with different dimensions. Both ports have an inner radius of .635mm, but port 1 has an outer radius of 2.29mm while port 2 has an outer radius of 3.05mm. The lower and left straight sides of the cavity have lengths L_1 = 43.18cm and L_2 = 21.59cm respectively and the upper and right sides have radius of curvature R_1 = 103cm and R_2 = 63.9cm respectively. By moving a perfectly conducting circular perturber with a diameter of 2.54cm to 95 different locations (shown as circles in Fig. 3.2) within the cavity, we construct our ensemble. The resulting impedances were simulated at 201 uniformly spaced frequencies from

5 to 7 GHz, inclusive. For this frequency range, we get that the effective loss parameter Q due to the ensemble averaging changes linearly from about 210 at 5 GHz to 300 at 7 GHz. The effective line-width to level spacing ratio α also increases linearly from about 0.95 to 1.35.

3.5.1 Single-port Tests

To test our predictions in the single-port case, we first confirm that at each frequency the impedances have a Lorentzian distribution, fitting to find the median and width. From the fit, we see that Eq. (3.50) does not converge quickly enough to be practical at a single frequency. However, we find that if we use frequency averaging and short orbits together, we regain universal statistics over a much narrower frequency band than was required with out previous theory [59] (i.e. if $\boldsymbol{Z}_R$ is used as in Eq. (3.4)). In addition, we confirm that as a function of frequency, the fitted $\boldsymbol{Z}_{avg}$ has the characteristic behavior of the impedance of a lossy cavity.

To test that the impedance is Lorentzian distributed at each frequency, we numerically find the three quartiles $Q_{(1,2,3)}(f)$ of the 95 sample impedances (denoted $Z_i(f)$) and thus find the sample median $Z_{med}(f) = Q_2(f)$ and the sample width $Z_{wid}(f) = Q_3(f) - Q_1(f)$. Assuming that $Z_{med}(f)$ and $Z_{wid}(f)$ are approximately the correct median and width, we can then find the phase of the normalized scattering matrix coefficient

$$\phi_i(f) = 2\tan^{-1}\left(\frac{Z(f) - Z_{med}(f)}{Z_{wid}(f)}\right). \tag{3.52}$$

For large N and with a Lorenzian distribution for $Z(f)$, $\phi_i(f)$ should be uniformly

distributed between $-\pi$ and π. We bin the numerical ϕ_i into 10 equal-sized bins and find the resulting χ^2 deviation from a uniform distribution. We then find the anticipated distribution of χ^2 by performing a Monte-Carlo statistical analysis on 402000 realizations of 95 Lorentzian random variables each, transforming them precisely as done in Eq. (3.52) and finding the resulting χ^2. Comparing the values of χ^2 for the simulation data and the Monte-Carlo distribution, we find that at the 95% confidence level, we can accept the Lorentzian hypothesis for 93% of our frequency impedance samples, while at the 99% confidence level, we can accept all of our impedance samples. These results are consistent with the data being distributed with a Lorentzian distribution at each frequency.

To test the semiclassical theory in the single-port case, rather than using the sample median and width we attempt to predict the median and width using Eqs. (3.5) and (3.50). In practice, we must eventually truncate the sum over semiclassical trajectories. We therefore define the truncated average impedance

$$\boldsymbol{Z}_{t,N_b} = \tilde{\boldsymbol{Z}}_R + 2\sum_{l=1}^{N_b} \vec{v}_1^{\dagger} \cdot \bar{\boldsymbol{T}}^l \cdot \vec{v}_1, \tag{3.53}$$

which is equivalent to the sum over all classical trajectories which bounce up to N_b times. Thus the normalized scattering phase we use to test our semiclassical theory is

$$\phi_{i,N_b}(f) = 2\tan^{-1}\left(-i\frac{Z_i(f) - iX_{t,N_b}(f)}{R_{t,N_b}(f)}\right), \tag{3.54}$$

where R_{t,N_b} and X_{t,N_b} are the real and imaginary parts of Z_{t,N_b}.

In Fig. 3.8, we compare Z_{t,N_b} to Z_{wid} for $N_b = 2, 5, 6$. We see that as N_b increases, the two terms becomes increasingly similar. $Z_{t,2}$ follows the frequency

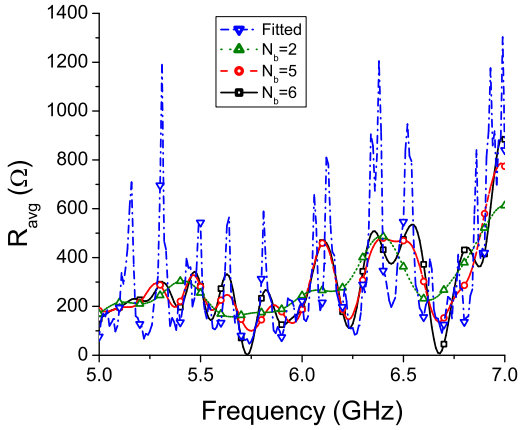

Figure 3.8: A comparison between the fitted width of the impedance distribution Z_{wid} at each measurement frequency and the semiclassical predictions for the widths due to short orbits which bounce up to 2, 5 or 6 times. By 6 bounces, the semiclassical prediction has begun to fit the gross features of the fitted widths but is far short of the number of orbits needed to fit the sharp spikes. In addition, Gibbs phenomenon has become a problem in the sixth bounce around 5.75 and 6.7 GHz with the semiclassical prediction dipping too close to zero. (Color online)

average of Z_{wid}. Also, despite the fact that Z_{wid} changes rapidly in frequency, consistent with the assumption that it is the real part of a lossy impedance, $Z_{t,5}$ and $Z_{t,6}$ have begun to fit even the large spikes in Z_{wid}. This strongly supports the validity of Eq. (3.50) and implies that with a sufficiently large number of bounces or a more random ensemble (such as including more perturbers or having a larger perturber), it may be possible to predict $\boldsymbol{Z}_{avg}$ at a single frequency. We have not yet confirmed this possibility.

In previous work, we found that normalizing the impedance with zero bounces (i.e. the radiation impedance $\boldsymbol{Z}_R$) was sufficient to get universal statistics if we sampled the impedances over a sufficiently wide frequency range. If the frequency

window was too narrow, however, we found systematic deviations from universal statistics. Even though we do not have enough terms in $\boldsymbol{Z}_{t,6}$ to experimentally find $\boldsymbol{Z}_{avg}$ semiclassically at a single frequency, we find that by combining short orbits and frequency averaging, we can get universal statistics over much narrower frequency ranges than previously.

To measure the deviation of the distribution of the measured ϕ_{i,N_n} from uniform, we introduce the χ^2 statistic. For a frequency window of width δf and centered at f_0, the χ^2 statistics is calculated by binning the ϕ_{i,N_b} from every realization and from every other frequency in the frequency window into ten equally sized bins from $-\pi$ to π. (We take every other frequency because the impedance values of adjacent frequencies are found to be strongly correlated.) The χ^2 statistic for this window is then given by

$$\chi^2 = \sum_{r=1}^{10} \frac{(N_r - \langle N_r \rangle)^2}{\langle N_r \rangle} \tag{3.55}$$

where N_r is the number of ϕ_{i,N_b} in the rth bin, and $\langle N_r \rangle$ is the expected value of N_r given a uniform distribution. The χ^2 statistic is chosen because it has approximately the same distribution independent of Δf.

In Fig. 3.9, we display the average χ^2 statistic from our sample for multiple values of N_b and different choices of window width. The averaging is performed over all frequency windows of the same width, including windows whose frequencies overlap. We see that for small window widths, increasing N_b systematically decreases the error. In addition, we also see that, up to a point, increasing the window size also decreases the error, but, once the error has leveled off, it decreases no fur-

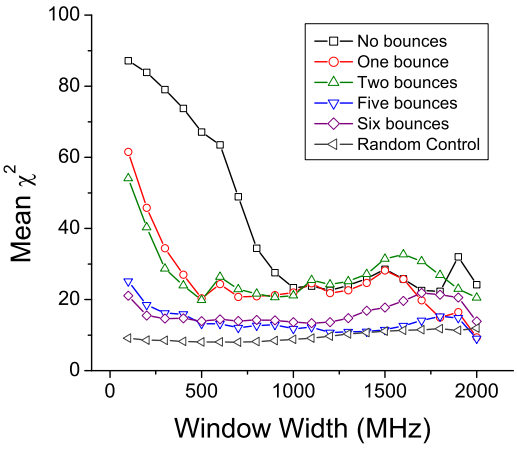

Figure 3.9: The average χ^2 deviation of the ϕ_{i,N_b} from the uniform distribution for different frequency windows and different choices of N_b. The χ^2 were calculated for all possible frequency windows with a given width and then averaged over all different window realizations. The random control was generated by a Monte-Carlo simulation of the χ^2 for uniformly distributed phases. Note that for the sixth bounce we exclude frequency windows in which the calculated $\boldsymbol{R}_{avg}$ falls below 0.1. (Color online)

ther. This is consistent with the frequency averaging effectively removing the longer orbits, making the improved statistics from the larger N_b irrelevant. In addition, for comparison we include the χ^2 statistics for a set of truly independent random phases and see that for the largest N_b and widest window widths, our results are statistically indistinguishable from true randomness.

At this point we note one caveat to our use of Eq. (3.54) relevant to Fig. 3.9. In Fig. 3.8, we see that $\boldsymbol{Z}_{t,6}$ drops almost to zero near 5.7GHz and 6.7GHz. In fact, if we continue to add bounces, $\boldsymbol{R}_{t,N_b}$ can actually become negative at some frequencies, which would represent gain in a lossy system and is unphysical. This

unphysical behavior occurs only because the sum in Eq. (3.50) has been truncated, but it badly distorts the calculation in Eq. (3.54) within the affected frequency ranges due to the abnormally small denominator. This occurs because our sum over orbits is effectively an attempt to expand a function with poles near the real axis in a Fourier series. Due to the rapidly changing features in $R_{avg,1,1}$, we get a form of Gibbs phenomenon, in which a Fourier series attempting to fit a discontinuous function systematically overshoots the fitted function. For the purposes of producing Fig. 3.9, we simply ignored frequency windows which contained frequencies such that $R_{t,6}(f) < 0.1 R_R(f)$. It may be possible to avoid this problem by using a smarter method to expand Eq. (3.45).

3.5.2 Two-port tests

To test the results from the two-port configuration, we first test the statistical properties of the diagonal elements of the two-port impedance, considered separately. From Eqs. (3.48) and (3.36), and remembering that the distribution of $\boldsymbol{\xi}$ is basis-independent, we find that the diagonal elements of the multi-port impedance, considered independently, should be Lorentian random variables with width $R_{avg,n,n}$ and median $X_{avg,n,n}$. Thus the diagonal elements of $\boldsymbol{Z}$ are susceptible to the same analysis used in the single-port case. When we perform this statistical analysis on both diagonal elements of $\boldsymbol{Z}$ considered independently, we get results essentially identical to those shown for the single-port case.

Because port 1 is in the same location for both the single-port and two-port

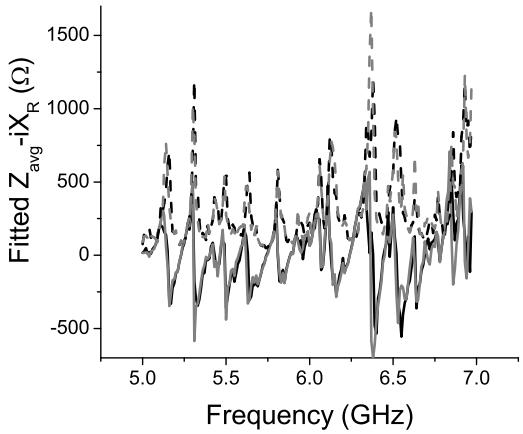

Figure 3.10: A comparison between the numerically found median (solid lines) and width (dashed lines) of the distribution of impedances at each frequency for the single-port simulated impedance (the black lines) and the (1,1) element of the two-port simulated impedance (the gray lines). Note that for clarity we have subtracted the radiation impedance of the single port from the medians of both sets of data.

simulations, our theory also predicts that the median and width of the distribution of $Z_{1,1}$ at a single frequency should be almost identical to the median and width of the single-port impedance distribution at the same frequency. The data is in agreement with this prediction as shown in Fig. 3.10 (note that, for the sake of clarity, we have subtracted the radiation reactance of the single port from the plotted medians of both sets of data).

The statistics of the two-port normalized impedance are more than the independent statistics of the diagonal elements; the elements of the 2×2 matrix $\boldsymbol{Z}$ are strongly correlated. All elements of $\boldsymbol{Z}$ go to infinity, for instance, when the frequency goes through a cavity resonance. One common way of expressing this is via the correlation between the eigenvalues of $\boldsymbol{\xi}$. The eigenvalues of $\boldsymbol{\xi}$ have the form

$\cot(\theta_n/2)$, where the distribution of the θ_n is given by [9]

$$P(\{\theta_n\}) \propto \prod_{n<m} |e^{i\theta_n} - e^{i\theta_m}|^\beta. \tag{3.56}$$

For the two-port impedance problem, this distribution simplifies to

$$P(\theta_1, \theta_2) = \frac{1}{4} \left| \sin\left(\frac{\theta_1 - \theta_2}{2}\right) \right|. \tag{3.57}$$

Thus to test our theory, we must fit or calculate $\boldsymbol{Z}_{avg}$, find the values of $\boldsymbol{\xi}$ for our sample data, diagonalize, and find the distribution of the differences between the resulting phases. We again use χ^2 to determine the goodness-of-fit with the definition from Eq. (3.55), but with $\langle N_r \rangle$ determined by integrating Eq. (3.57). As we did for the single-port case, we both fit to find the numerical $\boldsymbol{Z}_{avg}$ and use the semiclassical sum.

Numerically fitting $\boldsymbol{Z}_{avg}$ is more difficult for the two-port case than in the one-port case. We can find the diagonal elements of the fitted $\boldsymbol{Z}_{avg}$ simply by fitting the diagonal elements of $\boldsymbol{Z}$ to Lorenzians exactly as in the single-port case. Fitting the off-diagonal elements numerically is more complex because both the shape and width of the distribution of the off-diagonal elements of $\boldsymbol{Z}$ depend in a non-linear way on all the elements of $\boldsymbol{R}_{avg}$. Rather than attempting this more complex fit, we consider the rotated impedance matrix

$$\boldsymbol{O}\boldsymbol{Z}\boldsymbol{O}^T = i\boldsymbol{O}\boldsymbol{X}_{avg}\boldsymbol{O}^T + i(\boldsymbol{O}\sqrt{\boldsymbol{R}_{avg}}\boldsymbol{O}^T)(\boldsymbol{O}\boldsymbol{\xi}\boldsymbol{O}^T)(\boldsymbol{O}\sqrt{\boldsymbol{R}_{avg}}\boldsymbol{O}^T), \tag{3.58}$$

where $\boldsymbol{O}$ is a constant orthogonal matrix. Because the statistics of $\boldsymbol{\xi}$ are independent of basis, the diagonal elements of the rotated matrix $\boldsymbol{O}\boldsymbol{Z}\boldsymbol{O}^T$ will be Lorentzian distributed random variables with widths and means give by the diagonal elements

of $\boldsymbol{O}\boldsymbol{X}_{avg}\boldsymbol{O}^T$ and $\boldsymbol{O}\boldsymbol{R}_{avg}\boldsymbol{O}^T$. Thus if we make the simple choice

$$\boldsymbol{O} = \begin{pmatrix} \frac{1}{\sqrt{2}} & \frac{1}{\sqrt{2}} \\ -\frac{1}{\sqrt{2}} & \frac{1}{\sqrt{2}} \end{pmatrix}, \tag{3.59}$$

we find that the widths of the distribution of the diagonal elements of the rotated impedance are

$$(\boldsymbol{O}\boldsymbol{R}_{avg}\boldsymbol{O}^T)_{n,n} = \frac{R_{avg,1,1} + R_{avg,2,2}}{2} - (-)^n R_{avg,1,2}, \tag{3.60}$$

where $n = 1, 2$, and with corresponding logic for $\boldsymbol{X}_{avg}$. Thus to find $Z_{avg,1,2}$, we fit the diagonal elements of $\boldsymbol{O}\boldsymbol{Z}\boldsymbol{O}^T$ to Lorenzians and take the half difference between the fitted medians and widths for the different diagonal terms. This algorithm generalizes to larger numbers of ports by choosing $\boldsymbol{O}$ to rotate between the appropriate port indices. In the process, we also confirm that the diagonal elements of the rotated impedance are in fact Lorentzian distributed, providing further support for Eq. (3.48).

In Fig. 3.11, we show the results of this analysis. Rather than considering frequency windows, we simply consider the statistics of $|\theta_1 - \theta_2|$ at each individual frequency using different values of $\boldsymbol{Z}_{avg}$. We find that the numerically fitted $\boldsymbol{Z}_{avg}$ normalizes the data well, but not perfectly, with the range of χ^2 values falling well within acceptable bounds as determined by the theoretical distribution of χ^2, but systematically larger than would be expected from true randomness. For the truncated sums, however, the story is rather different. We see that at many frequencies, no corrections are needed at all to get good statistics. Some frequencies, however, have large deviations from Eq. (3.57). That these deviations are caused

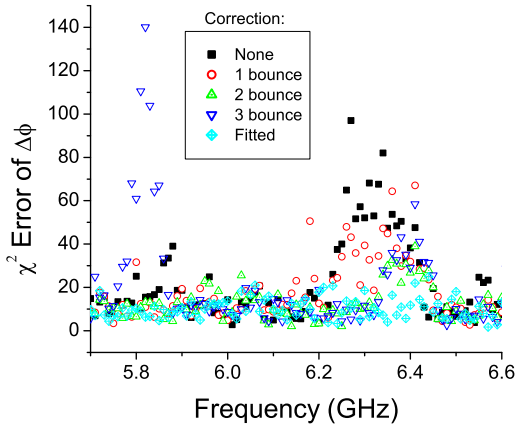

Figure 3.11: A comparison between the universality of the phases of $\boldsymbol{\xi}$ as extracted using different methods for normalizing the two-port impedance data. All data shown is the χ^2 statistics for fitting the different between phases to Eq. (3.57). The gray lines represent error of the data normalized using the semiclassical impedance sum. The solid line represents the phase difference statistics, but at each frequency using the fitted value for $\boldsymbol{Z}_{avg}$, where the fitting parameters are found as described in the text. (Color online)

by short orbits is demonstrated by the fact that, as we add 1 and 2 bounces to the semiclassical $\boldsymbol{Z}_{avg}$, the deviations initially become smaller, almost reaching the level of noise. Unfortunately, adding longer orbits does not improve the situation; they leave the statistics either unchanged or markedly worse. The reasons for this are unclear but are likely due to a combination of the Gibbs phenomenon observed in Sec. 3.5.1 and the tendency of some impedance matrices to be poorly conditioned due to systematically large values of $\cot(\theta_n/2)$.

Thus we have confirmed many of the predictions of the extended random coupling model, including the approximate independence of the statistics of the diagonal elements of $\boldsymbol{Z}$, the invariance of the distribution under rotation, and the level spacing statistics for pairs of eigenvalues of $\boldsymbol{\xi}$.

3.6 Adding Loss

In practice, no real cavity will be truly lossless. For non-zero frequencies, even cavities with superconducting boundaries have loss due to interactions between microwave photons and quasiparticles. In quantum mechanical systems, there will always be dephasing, which is functionally equivalent to loss [10]. In this section we therefore address the effects loss has on our theory.

From Maxwell's equations, we derived in previous work [59] that going from lossless to uniformly lossy is performed by the transformation $k \to k + i\alpha$, where $\alpha = k/(2Q)$ and $Q \gg 1$ is the loss parameter of the closed cavity. Performing this analytical continuation takes some care. The function that must be explicitly continued analytically to obtain universal statistics of the sort we found previously is the normalized impedance $\boldsymbol{\xi}$, given by

$$i\boldsymbol{\xi} = \boldsymbol{R}_{avg}^{-1/2} \left(\boldsymbol{Z} - i\boldsymbol{X}_{avg}\right) \boldsymbol{R}_{avg}^{-1/2}. \tag{3.61}$$

Because $\boldsymbol{R}_{avg}$ and $\boldsymbol{X}_{avg}$ appear independently in Eq. (3.61), we must analytically continue each independently. Because taking the real and imaginary parts of non-constant functions is not an analytic operation, for lossy systems $\boldsymbol{R}_{avg}$ and $\boldsymbol{X}_{avg}$ are not real but rather the analytic continuation of the real and imaginary part of the lossless $\boldsymbol{Z}_{avg}$ on the real axis. These analytic continuations are unique.

To find this analytic continuation for the microwave billiards used in our experiments, it is necessary to explicitly find the real and imaginary parts of $\boldsymbol{Z}_{avg}$.

For our microwave billiard system, we find that

$$\boldsymbol{R}_{avg} = \boldsymbol{R}_R + \boldsymbol{R}_R^{1/2}\boldsymbol{\rho}\boldsymbol{R}_R^{1/2} \tag{3.62}$$

$$\boldsymbol{X}_{avg} = \boldsymbol{X}_R + \boldsymbol{R}_R^{1/2}\boldsymbol{\chi}\boldsymbol{R}_R^{1/2} \tag{3.63}$$

where the $M \times M$ matrices $\boldsymbol{\rho}$ and $\boldsymbol{\chi}$ have the elements

$$\rho_{n,m} = \sum_{b(n,m)} p_{b(n,m)} \sqrt{D_{b(n,m)}} \cos\left(k\left(L_{p,n} + L_{p,m} + L_{b(n,m)}\right) - \pi/4\right), \tag{3.64}$$

$$\chi_{n,m} = \sum_{b(n,m)} p_{b(n,m)} \sqrt{D_{b(n,m)}} \sin\left(k\left(L_{p,n} + L_{p,m} + L_{b(n,m)}\right) - \pi/4\right), \tag{3.65}$$

where we have made the empirically observed substitution $\Delta\phi_n = kL_{p,n}$, $L_{p,n}$ is observed to be a port-dependent constant, and $L_{b(n,m)}$ is the length of the trajectory $b(n,m)$, where we have used that for billiards, $S_{b(n,m)}(k) = kL_{b(n,m)}$.

Because $\boldsymbol{Z}_R$ and $D_{b(n,m)}$ change slowly in frequency compared to the level spacing, they are approximately independent of α and thus equal to their lossless counterparts. Thus the analytic continuations of $\boldsymbol{R}_{avg}$ and $\boldsymbol{X}_{avg}$ consist of keeping the forms of Eqs. (3.62)-(3.65) unchanged but allowing k to become complex.

After performing this continuation, $\boldsymbol{\xi}$ will no longer be real. However the distributions of the real and imaginary parts of $i\boldsymbol{\xi}$ have been found as a function of the loss parameter, [23, 47] and, for low-loss systems, we expect the distribution to be approximately universal. The only difficulty with this analytic continuation is that the sum in Eq. (3.49) will not necessarily converge if the loss parameter is too high. In such a case, it is necessary to perform the analytical continuation on the form of $\boldsymbol{Z}_{avg}$ given in Eq. (3.45). At this time, we have not attempted this, but we anticipate that it will require evaluating the denominator in Eq. (3.45) via a method other than short orbits, a poosible subject of further research.

We have experimentally tested this theory in the one-port case for a microwave quarter-bowtie billiard described in previous work for frequencies from 6 to 18 GHz [57]. The primary difficulty in applying Eqs. (3.5) and (3.50) over this frequency range is the fact that the loss parameter is not constant as a function of frequency. However, our theory predicts that the phase of the normalized scattering parameter s will be uniformly distributed independent of the loss parameter [59], where s is given by

$$s = \frac{i\xi - 1}{i\xi + 1}. \tag{3.66}$$

Thus by fitting the distribution of the phase of the normalized scattering parameter to the uniform distribution, we can again find the χ^2 statistic for various frequency windows and different choices for the number of bounces before truncation N_b. We have performed this experiment with a lossy cavity and found results qualitatively similar to Fig. 3.9 [57].

3.7 Conclusions

In this chapter, we have shown that the random coupling model, Ref. [60] and Eq. (3.4), can be extended to take into account system specific short orbits that affect the statistical features of the system. From the numerically and experimentally observed deviations of our results from universality, we anticipated that interactions between the walls and the port that were not sufficiently changed from realization to realization would result in corrections to our model. We then derived a model that could predict such corrections. Numerically and experimentally, we found that the

improved model resulted in statistically significant improvement when fitting to the random coupling model, effectively reducing the deviations to the level of noise. In addition, we developed utilizations of several mathematical tools, including Prange's semiclassical version of Bogomolny's $\boldsymbol{T}$ operator, that could be fruitful in further study of chaotic cavities and wave-chaotic systems with known dynamics in general.

Appendix A

Finding the Distribution of ξ_n for Small γ_n

To find the distribution of ξ_n defined in Eq. (2.23) for small γ_n, we exploit the fact that, in a two-port system with the ports identical and described by Random Matrix Theory, the diagonal elements of the normalized impedance matrix each have the same statistics as the single-port normalized impedance. Then using the exact statistics of the two-port RMT impedance, we can find the statistics of the one-port impedance (2.19).

We see this by first writing the elements of the two-port normalized impedance matrix as a sum, analogous to Eq. (2.10),

$$\xi_{i,j} = -\frac{j}{\pi} \sum_n \frac{w_{i,n} w_{j,n}}{k^2 - k_n^2}, \tag{A.1}$$

where the $w_{i,n}$ are independent Gaussian random variables and the k_n^2 have the statistics of the eigenvalues of a GOE random matrix.

As shown in previous work [60], the 2x2 matrix ξ has the following statistics: its eigenvalues $\tan\theta_1$, and $\tan\theta_2$ have a joint pdf,

$$P(\theta_1, \theta_2) \propto \left| \sin\left(\frac{\theta_2 - \theta_1}{2} \right) \right|, \tag{A.2}$$

and its eigenvectors $(\cos\nu, \sin\nu)$ and $(-\sin\nu, \cos\nu)$ have ν uniformly distributed and independent of θ_1 and θ_2. Consequently, a diagonal element of ξ can also be parameterized as

$$\xi_{i,i} = \cos^2\eta \tan\theta_1 + sin^2\eta \tan\theta_2. \tag{A.3}$$

Comparing Eqs. (A.1) and (A.3), we see that the singularity at $k = k_n$ in Eq. (A.1) is matched by either θ_1 or θ_2 going through $\pi/2$; for specificity we assume that it is θ_1. For small γ_n, corresponding to small w_n^2, the coefficient of the singularity is small, which corresponds to $\cos^2 \eta \approx 0$. Thus, for small γ_n, ξ_n has the statistics given by

$$\xi_n = \tan \theta_2|_{\theta_1=\pi/2} \tag{A.4}$$

which inserted into Eq. (A.2) produces the pdf for $\psi_n = \tan^{-1} \xi_n = \theta_2$

$$P(\psi_n) = \frac{\cos \psi_n}{2} \tag{A.5}$$

Numerically we confirm this by generating a single 600x600 element matrix from the Gaussian Orthogonal Ensemble and calculating and scaling the eigenvalues to get an appropriate spectrum. We then repeatedly generate 600 realizations of 600 coupling constants and use them to calculate 360,000 realizations of X_n, which we then normalize to calculate ψ_n. The resulting statistics are demonstrated in Fig. A.1.

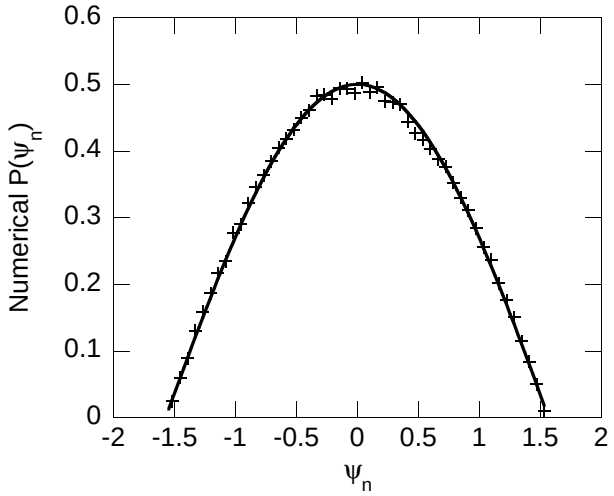

Figure A.1: A comparison of a numerically-generated pdf of ψ_n ('+' symbols) with the anticipated result from Eq. (A.5), $\cos(\psi_n)/2$ (the solid line).

Appendix B

Finding the Cumulants of $\bar{P}_{\rm ref}$

To obtain Eq. (2.50), we note that the cumulant generating function of $\bar{P}_{\rm ref}$ obeys

$$\begin{aligned} g(h) &= \log\left(\left\langle \exp\left(h\sum_n \frac{\left|2\pi\Delta\omega\bar{V}_{\rm inc}(\omega_n)\right|^2}{Z_0}\frac{\gamma_n^2}{\Delta\omega^2}e^{-2\gamma_n t}\right)\right\rangle\right) \\ &= \sum_n \log\left(\left\langle \exp\left(h\frac{\left|2\pi\Delta\omega\bar{V}_{\rm inc}(\omega_n)\right|^2}{Z_0}\frac{\gamma_n^2}{\Delta\omega^2}e^{-2\gamma_n t}\right)\right\rangle\right). \end{aligned} \tag{B.1}$$

This result is a specific example of a general property of cumulants [37]: The mth cumulant of a sum of independent variables is the sum of the mth cumulants of the single variables. Thus, in analogy to Eq. (2.48), we define the cumulant-generating function and the cumulants $\tilde{\kappa}_p$ for each term in the sum in Eq. (B.1) as

$$\tilde{g}(q) = \log\left(\left\langle \exp\left(q\frac{\gamma_n^2}{\Delta\omega^2}e^{-2\gamma_n t}\right)\right\rangle\right) = \sum_{p=1}^{\infty}\tilde{\kappa}_p\frac{q^p}{p!}, \tag{B.2}$$

and by matching coefficients of h^m in Eq. (B.1), we get that

$$\kappa_m = \tilde{\kappa}_m\sum_n \frac{\left|2\pi\Delta\omega\bar{V}_{\rm inc}(\omega_n)\right|^{2m}}{Z_0^m}. \tag{B.3}$$

All that is left is to find the long-term behavior for $\tilde{\kappa}_m$. To do this, we note that we can rewrite the average exponential in Eq. (B.2) as

$$\left\langle \exp\left(q\frac{\gamma_n^2}{\Delta\omega^2}e^{-2\gamma_n t}\right)\right\rangle = 1 + \sum_{n=1}^{\infty}\frac{q^n\mu_n}{n!}. \tag{B.4}$$

Because q is a dummy variable which can be arbitrarily small, we can also expand the logarithm in Eq. (B.2) to get that

$$\sum_{p=1}^{\infty} \tilde{\kappa}_p \frac{q^p}{p!} = \sum_{n=1}^{\infty} \frac{q^n \mu_n}{n!} - \frac{1}{2}\left(\sum_{n=1}^{\infty} \frac{q^n \mu_n}{n!}\right)^2 + \frac{1}{3}\left(\sum_{n=1}^{\infty} \frac{q^n \mu_n}{n!}\right)^3 - \ldots. \tag{B.5}$$

By matching coefficients of q^p on both sides of Eq. (B.5), we find that [37],

$$\tilde{\kappa}_1 = \mu_1, \tag{B.6}$$

$$\tilde{\kappa}_2 = \mu_2 - \mu_1^2, \tag{B.7}$$

$$\tilde{\kappa}_m = \mu_m - m\mu_{m-1}\mu_1 + \ldots - (-1)^m \mu_1^m, \tag{B.8}$$

where the elided terms are products of different μ_n such that the indices add up to m. For large t, all of these polynomial terms are small compared μ_m. We can see this by noting that $\mu_m \propto (t\Delta\omega)^{-2m-1/2}$. Thus

$$\frac{\mu_m}{\mu_l \mu_{m-l}} \propto (t\Delta\omega)^{1/2}, \tag{B.9}$$

where the proportionality constant can be shown to be order 1. For every extra factor of μ_l included in a term, we pick up an extra factor of $(t\Delta\omega)^{1/2}$ in the numerator of the ratio between μ_m and that term. Thus for large times we have that μ_m is much greater than any of the other polynomial terms in Eq. (B.8) and therefore

$$\tilde{\kappa}_m \approx \mu_m. \tag{B.10}$$

Combining Eqs. (2.39), (B.3), and (B.10), we get Eq. (2.50).

Appendix C

The time domain code

In this section, we describe the time domain code used to create the realizations in Fig. 2.1. This code effectively solves Eq. (2.1) using the approximations that were inserted into Eq. (2.8) to produce Eq. (2.10). In addition, it makes use of a slowly varying envelope approximation which greatly increases the size of the numerically stable time-step and also transforms Maxwell's Equations into Schrödinger's Equation.

To solve Eq. (2.1), we first find expand $V(x, y, t)$ in terms of the eigenfunctions of the closed system

$$\bar{V}_T(x, y, t) = \sum_n \frac{\tilde{c}_n(t)\phi_n(x, y)}{\sqrt{\int d\theta \, |u(\vec{w}_0 c)|^2}}. \tag{C.1}$$

We note that the $c_n(\omega)$ from Eq. (2.6) are proportional to Fourier transforms of the $\tilde{c}_n(t)$. Substituting Eq. (C.1) into Eq. (2.1) and using the orthonormality of the ϕ_n, we get

$$\frac{1}{c^2}\frac{d^2}{dt^2}\tilde{c}_n(t) + k_n^2\tilde{c}_n(t) = \frac{8\pi R_R(\omega_0 c)}{\omega_0}\frac{dI(t)}{dt}\left[\frac{\int dx\, dy\, u\phi_n}{\sqrt{\int d\theta \, |u(\vec{w}_0 c)|^2}}\right], \tag{C.2}$$

where we have used the definition of radiation resistance from Ref. [59, Eq. 19] to remove the factor $h\mu$. The value of ω_0 is the modulation frequency used in the envelope approximation (See Eqs. (C.3) and (C.4)).

To apply the envelope approximation, we assume that

$$I(t) = I_{\text{env}}(t)e^{j\omega_0 t} \tag{C.3a}$$

$$\tilde{c}_n(t) = d_n(t)e^{j\omega_0 t} \tag{C.3b}$$

where

$$\frac{d}{dt}I_{\text{env}}(t) \ll \omega_0 I_{\text{env}}(t) \tag{C.4a}$$

$$\frac{d}{dt}d_m(t) \ll \omega_0 d_m(t). \tag{C.4b}$$

$$\frac{d^2}{dt^2}d_m(t) \ll \omega_0 \frac{d}{dt}d_m(t). \tag{C.4c}$$

Then we drop all terms which are small, noting that $k_n \approx \omega_0/c$, which implies that $k_n^2c^2 - \omega_0^2 = (k_nc - \omega_0)(k_nc + \omega_0)$ is on the order of ω_0. This gives us

$$\left[\frac{2j\omega_0}{c^2}\frac{\partial}{\partial t} + (k_n^2 - \frac{\omega_0^2}{c^2})\right] d_n(t) = 8j\pi R_R(\omega_0 c) I_{\text{env}}(t) \left[\frac{\int dx\, dy\, u\phi_n}{\sqrt{\int d\theta\, |u(\vec{w}_0 c)|^2}}\right] \tag{C.5}$$

Again we replace the overlap integral between ϕ_n and u with the statistical approximation found in Ref. [59, Eq. 14] to get

$$\left[\frac{2j\omega_0}{c^2}\frac{\partial}{\partial t} + (k_n^2 - \frac{\omega_0^2}{c^2})\right] d_n(t) = \sqrt{8\Delta} w_n j R_R(\omega_0 c) I_{\text{env}}(t). \tag{C.6}$$

Similarly, combining Eqs. (C.1) and (2.2) and using the envelope approximation throughout, we get

$$V_{\text{env}}(t) = \sum_n V_n(t), \tag{C.7}$$

where $V_{\text{env}}(t)$ is the envelope of $V(t)$ in analogy to Eq. (C.3) and

$$V_n(t) = \frac{\sqrt{\Delta}}{4\pi} d_n(t) w_n. \tag{C.8}$$

Solving Eqs. (2.3) and (2.4) for $I(t)$ by eliminating $V_{\text{ref}}(t)$ and inserting the result into Eq. (C.6), we get

$$\left[\frac{2j\omega_0}{c^2}\frac{\partial}{\partial t} + (k_n^2 - \frac{\omega_0^2}{c^2})\right] V_n(t) = j\frac{\Delta R_R(\omega_0 c) w_n^2}{\sqrt{2}\pi Z_0} \left(2V_{i,\text{env}}(t) - \sum_m V_m(t)\right), \tag{C.9}$$

where $V_{i,\mathrm{env}}(t)$ is the envelope of $V_{\mathrm{inc}}(t)$ in direct analogy to Eq. (C.3).

Equation (C.9) is a set of complex first order linear differential equations analogous to Shrödinger's equation. By truncating the spectrum to a finite number of modes, it is possible to solve Eq. (C.9) numerically via standard numerical integration techniques. In our case, we choose forth-order Runga Kutta. We generate the values of $k_n^2 - k_0^2$ by generating 600x600 random matrices from the Gaussian Orthogonal Ensemble, finding the spectrum, and unfolding it such that the $k_n^2 - k_0^2$ have a uniform density. We also generate the 600 w_n as Gaussian random variables with 0 mean and width 1. All of the remaining variables (including the initial conditions) are physical parameters that must be set to match the situation we wish to simulate.

For the runs displayed in this paper, we chose $R_R(\omega_0 c)/Z_0 = 1$, $\omega_0 = 22.5$ GHz, and $\Delta = 10$ m^{-2}. The k_n were chosen to lie between ≈ 51 m^{-1} and 93 m^{-1}. For initial conditions, $V_n(0) = 0$. The envelope of the incident pulse, $V_{i,\mathrm{env}}$, had the form

$$V_{i,\mathrm{env}}(t) = e^{-(t\sigma_\omega - 5)^2/2} \tag{C.10}$$

with $\sigma_\omega = 150$ MHz.

Bibliography

[1] S. Adam, P.W. Brouwer, J.P. Sethna, and X. Waintal. Enhanced mesoscopic fluctuations in the crossover between random-matrix ensembles. *Phys. Rev. B*, 66, 2002.

[2] Y. Alhassid. The statistics theory of quantum dots. *Rev. Mod. Phys.*, 72(4):895–968, 2000.

[3] H. Alt, H.-D. Gräf, H. L. Harney, R. Hofferbert, H. Lengeler, A. Richter, P. Schardt, and H. A. Weidenmüller. Gaussian orthogonal ensemble statistics in a microwave stadium billiard with chaotic dynamics: Porter-thomas distribution and algebraic decay of time correlations. *Phys. Rev. Lett.*, 74(1):62–65, 1995.

[4] Nathan Argaman, Yoseph Imry, and Uzy Smilansky. Semiclassical analysis of spectral correlations in mesoscopic systems. *Phys. Rev. B*, 47:4440 – 4457, 1993.

[5] C.W.J. Beenakker. Random-matrix theory of quantum transport. *Rev. Mod. Phys.*, 69:731–808, 1997.

[6] M. V. Berry. Semiclassical theory of spectral rigidity. *Proc. R. Soc. London Ser. A*, 400, 1985.

[7] R. Blumel, I. H. Davidson, W. P. Reinhardt, H. Lin, and M. Sharnoff. Quasilinear ridge structures in water surface waves. *Phys. Rev. A*, 45:2641–1644, 1992.

[8] E B Bogomolny. Semiclassical quantization of multidimensional systems. *Nonlinearity*, 5:805–866, 1992.

[9] P. W. Brouwer. Generalized circular ensemble of scattering matrices for a chaotic cavity with nonideal leads. *Phys. Rev. B*, 51:16878 – 16884, 1995.

[10] P. W. Brouwer and C. W. J. Beenakker. Voltage-probe and imaginary-potential models for dephasing in a chaotic quantum dot. *Phys. Rev. B*, 55:4695, 1997.

[11] Evgeny N. Bulgakov, Vctor A. Gopar, Pier A. Mello, and Ingrid Rotter. Statistical study of the conductance and shot noise in open quantum-chaotic cavities: Contribution from whispering gallery modes. *Phys. Rev. B*, 73:155302, 2006.

[12] M. Buttiker. Role of quantum coherence in series resistors. *Phys. Rev. B*, 33:3020 – 3026, 1986.

[13] M. Buttiker. Time-dependent transport in mesoscopic structures. *J. Low Temp. Phys.*, 118(5-6):519–542, 2000.

[14] P. A. Chinnery and V. F. Humphrey. Experimental visualization of acoustic resonances within a stadium-shaped cavity. *Phys. Rev. E*, 53:272–276, 1996.

[15] Paul A. Chinnery, Victor F. Humphrey, and Carolyn Beckett. The schlieren images of two-dimensional ultrasonic fields and cavity resonances. *J. Acoust. Soc. Am.*, 101:250–256, 1997.

[16] Frank-Michael Dittes. The decay of quantum systems with a small number of open channels. *Phys. Rep.*, 339:215–316, 2000.

[17] Frank-Michael Dittes, H. L. Harney, and A. Muller. Nonexponential decay of a stochiastic one-channel system. *Phys. Rev. A*, 45(2):701–705, 1992.

[18] Eyal Doron and Uzy Smilansky. Some recent developments in the quantum theory of chaotic scattering. *Nucl. Phys. A*, 545:455–466, August 1992.

[19] Freeman J. Dyson. Statistical theory of the energy levels of complex systems. i. *J. Math. Phys.*, 3, 1962.

[20] C. Ellegaard, T. Guhr, K. Lindemann, H. Q. Lorensen, J. Nygard, and M. Oxborrow. Spectral statistics of acoustic resonances in aluminum blocks. *Phys. Rev. Lett.*, 75:1546–1549, 1995.

[21] Schmul Fishman, Bertrand Georgeot, and Richard Prange. Fredholm method for scars. *J. Phys. A: Math. Gen.*, 29:919–937, 1996.

[22] K. M. Frahm, H. Schomerus, M. Patra, and C. W. J. Beenakker. Large petermann factor in chaotic cavities with many scattering channels. *Europhys. Lett.*, 49:48, 2000.

[23] Y. V. Fyodorov and D. V. Savin. Statistics of impedance, local density of states, and reflection in quantum chaotic systems with absorption. *JETP Letters*, 80:725729, 2004.

[24] Yan V. Fyodorov and Hans-Jürgen Sommers. Statistics of resonance poles, phase shifts and time delays in quantum chaotic scattering: Random matrix approach for systems with broken time-reversal invariance. *J. Math. Phys.*, 38:1918–1981, 1997.

[25] Bertrand Georgeot and Richard E. Prange. Exact and quasiclassical fredholm solutions of quantum billiards. *Phys. Rev. Lett.*, 74(15):2851 – 2854, 1995.

[26] Bertrand Georgeot and Richard E. Prange. Fredholm theory for quasiclassical scattering. *Phys. Rev. Lett.*, 74:4110–4113, 1995.

[27] Sven Gnutzmann and Uzy Smilansky. Quantum graphs: Applications to quantum chaos and universal spectral statistics. *Advances in Physics*, 55:527–625, 2006.

[28] T. Gorin, T. Prosen, T. H. Seligman, and M. Znidaric. Dynamics of loschmidt echoes and fidelity decay. *Phys. Rep.-Rev. Sec. Phys. Lett.*, 435:33–156, 2006.

[29] Thomas Guhr, Axel Müller-Groeling, and Hans A. Weidenmüller. Random-matrix theories in quantum physics: common concepts. *Phys. Rep.*, 299(4-6):189–425, 1998.

[30] Martin C. Gutzwiller. Periodic orbits and classical quantization conditions. *J. Math. Phys.*, 12, 1971.

[31] Martin C. Gutzwiller. *Chaos in Classical and Quantum Mechanics*. Springer-Verlag, 1990.

[32] Fritz Haake. *Quantum Signatures of Chaos*. Springer, 2 edition, 2000.

[33] Paul R. Halmos. *Measure Theory*. Springer, 1978.

[34] James A. Hart, Thomas M. Antonsen, and Edward Ott. The effect of short ray trajectories on the scattering statistics of wave chaotic systems. Unpublished. Available at http://arxiv1.library.cornell.edu/abs/0906.4086, June 2009.

[35] James A. Hart, Thomas M. Antonsen, and Edward Ott. Scattering a pulse from a chaotic cavity: Transitioning from algebraic to exponential decay. *Phys. Rev. E*, 2009.

[36] Sameer Hemmady, James Hart, Xing Zheng, Thomas M. Antonsen, Edward Ott, and Steven M. Anlage. Experimental test of universal conductance fluctuations by means of wave-chaotic microwave cavities. *Phys. Rev. B*, 74, 2006.

[37] J. F. Kenney and E. S. Keeping. *Mathematics of Statistics*, volume 2. Van Nostrand, Princeton, NJ, second edition, 1951.

[38] T. Kottos and U. Smilansky. Quantum graphs: a simple model for chaotic scattering. *J. Phys. A*, 36:3501–3524, 2003.

[39] Tsampikos Kottos and Uzy Smilansky. Chaotic scattering on graphs. *Phys. Rev. Lett.*, 85:968–971, 2000.

[40] P. E. Lindelof, J. Norregaard, and J. Hanberg. New light on the scattering mechanisms in si inversion layers by weak localization experiments. *Phys. Scr.*, T14:17–26, 1986.

[41] Pier A. Mello and Harold U. Baranger. Short paths and information theory in quantum chaotic scattering: transport through quantum dots. *Europhys. Lett.*, 33:465–470, 1996.

[42] Pier A. Mello and Harold U. Baranger. Interference phenomena in electronic transport through chaotic cavities: an information-theoretic approach. *Waves in Random Media*, 9:105–146, 1999.

[43] Pier A. Mello, Pedro Pereyra, and Thomas H. Seligman. Information theory and statistical nuclear reactions. i. general theory and applications to few-channel problems. *Ann. Phys.*, 161:254–275, 1985.

[44] John M Nieminen. Eigenvalue spacing statistics of a four-matrix model of some four-by-four random matrices. *J. Phys. A: Math. Theor.*, 42, 2009.

[45] A. Pandey and M. L. Mehta. Gaussian ensembles of random hermitian matrices intermediate between orthogonal and unitary ones. *Communications in Mathematical Physics*, 87:449–468, 1983.

[46] C. E. Porter. *Statistical Theory of Spectra: Fluctuations*. Academic Press, New York, NY, 1965.

[47] D. V. Savin, H.-J. Sommers, and Y. V. Fyodorov. Universal statistics of the local greens function in wave chaotic systems with absorption. *JETP Letters*, 82:544–548, 2005.

[48] H. Schomerus, K. M. Frahm, M. Patra, and C. W. J. Beenakker. Quantum limit of the laser linewidth in chaotic cavities and statistics of residues of scattering matrix poles. *Physica A*, 278:469–496, 2000.

[49] H. Schomerus and J. Tworzydlo. Quantum-to-classical crossover of quasi-bound states in open quantum systems. *Phys. Rev. Lett.*, 93:154102, 2004.

[50] Dong-Ho Wu J. S. A. Bridgewater Seok-Hwan Chung, Ali Gokirmak and Steven M. Anlage. Measurement of wave chaotic eigenfunctions in the time-reversal symmetry-breaking crossover regime,. *Phys. Rev. Lett.*, 85:2482–2484, 2000.

[51] Hans-Jürgen Sommers, Yan V Fyodorov, and Mikhail Titov. S-matrix poles for chaotic quantum systems as eigenvalues of complex symmetric random matrices: from isolated to overlapping resonances. *J. Phys. A: Math. Theor.*, 32:L77–L85, 1999.

[52] H.-J. Stockmann and J. Stein. quantum chaos in billiards studied by microwave absorption. *Phys. Rev. Lett*, 64:2215–2218, 1990.

[53] F. G. Tricomi. *Integral Equations*. Dover Publications, Inc., 1985.

[54] R. L. Weaver. Spectral statistics in elastodynamics. *J. Acoust. Soc. Am.*, 85, 1989.

[55] Andr Weil. *Basic Number Theory*. Academic Press, 1971.

[56] Eugene P. Wigner. Characteristic vectors of bordered matrices with infinite dimensions. *Ann. of Math.*, 62:548–564, 1955.

[57] Jen-Hao Yeh, Elliot Bradshaw, James Hart, Thomas Antonsen, Edward Ott, and Steven Anlage. Unpublished, May 2009.

[58] Xing Zheng. *Statistics of Impedance and Scattering Matrices in Chaotic Microwave Cavities: The Random Coupling Model*. PhD thesis, University of Maryland, 2005. http://hdl.handle.net/1903/2920.

[59] Xing Zheng, T. M. Antonsen, and E. Ott. Statistics of impedance and scattering matrices in chaotic microwave cavities: Single channel case. *Electromagnetics*, 26:3–35, 2006.

[60] Xing Zheng, T. M. Antonsen, and E. Ott. Statistics of impedance and scattering matrices of chaotic microwave cavities with multiple ports. *Electromagnetics*, 26:37–55, 2006.

[61] I. V. Zozoulenko and T. Blomquist. Time-resolved dynamics of electron wave packets in chaotic and regular quantum billiards with leads. *Phys. Rev. B*, 67:085320, 2003.